Available online at www.sciencedirect.com

SCIENCE DIRECT®

ELSEVIER

International Journal of Impact Engineering 32 (2005) 473–507

INTERNATIONAL JOURNAL OF IMPACT ENGINEERING

www.elsevier.com/locate/ijimpeng

Laser shock compression of copper and copper–aluminum alloys

Matthew S. Schneider[a], Bimal Kad[a], Daniel H. Kalantar[b], Bruce A. Remington[b], Edward Kenik[c], H. Jarmakani[a], Marc A. Meyers[a,*]

[a]*Materials Science and Engineering, University of California, San Diego, MC 0418, La Jolla, CA 92093, USA*
[b]*Lawrence Livermore National Laboratory, Livermore, CA 94450, USA*
[c]*Oak Ridge National Laboratory, Oak Ridge, TN 37831, USA*

Received 20 November 2004; received in revised form 20 May 2005; accepted 22 May 2005
Available online 25 August 2005

Abstract

Copper and copper aluminum (2 and 6 wt% Al) with orientations [0 0 1] and [1 3 4] were subjected to high intensity laser shocks (energy levels of 40–300 J; energy densities of 15–70 MJ/m^2 and durations below 10 ns). In situ X-ray diffraction and VISAR wave profile measurements were used to study the response of the lattice to the shock. Recovered samples were characterized by transmission electron microscopy in order to study the defects within the lattice. The results are rationalized in terms of a criterion in which slip and twinning are considered as competing mechanisms. The slip-twinning transition is determined quantitatively and predicted as a function of orientation, temperature, and stacking fault energy (determined by the Al content of the alloy). A constitutive description is applied to the two orientations and differing compositions, incorporating both slip and twinning in terms of orientation, stacking fault energy, temperature, and strain rate. The threshold stress is calculated, considering the effect of shock heating. The constitutive description provides calculated thresholds in pure copper: 18 GPa for [0 0 1] and 25 GPa for [1 3 4]. The experimentally determined threshold twinning stress for pure copper in the [0 0 1] orientation is 25 GPa, whereas the one for the [1 3 4] orientation is between 40 and 60 GPa. The predictions are in agreement with experiments. It also provides thresholds for the Cu–Al alloys.

The growth of voids in incipient spalling is modeled by dislocation loop emission from the void surface. The first dislocation-based void growth mechanism, proposed by Lubarda et al. [Acta Mat 2004; 52: 1397]

---

*Corresponding author. Fax: +1 858 534 5698.
E-mail address: mameyers@ucsd.edu (M.A. Meyers).

0734-743X/$ - see front matter © 2005 Elsevier Ltd. All rights reserved.
doi:10.1016/j.ijimpeng.2005.05.010

is reviewed and extended to three dimensions. It has a generality rendering it applicable to a broad range of strain rates.

© 2005 Elsevier Ltd. All rights reserved.

Keywords: Laser; Laser shock; Compression; Shock compression; Copper; Void; Void growth; Dislocation; Loop emissions; High strain rate

---

1. Introduction

The effects of shock waves on metals have been studied for over 50 years [1]. During this time, most of the experiments used explosives and flyer plates as the means of creating the compression pulse. The generation of shock pulses in metals from laser-pulse induced vaporization at the surface was first demonstrated by Askaryon and Morez [2] in 1963. Shortly thereafter, White [3] and others [4–6] advanced this technique and postulated that lasers could be used to obtain Hugoniot data for a broad range of pressures. The use of surfaces covered by a laser-transparent overlay was introduced by Anderholm [7]; this enabled the confinement of the vapor products resulting in an increase of the peak pressure of the shock incident on the metal.

The shock pulses are created due to the rapid heating of the surface from the photon bombardment of the material. The surface heats and expands, forming a plasma. Because of the rapid heating and thermal expansion, the front of the material is shock compressed at times on the order of nanoseconds. This pulse then propagates through the material as a shock wave. The heat effects from the laser irradiation are limited to the first few atomic planes. Fig. 1(a)–(d) shows several modes by which lasers can be used to shock compress materials: the direct drive, plasma confining overlay, laser driven flyer plates, and the *hohlraum* effect. Shock amplitudes as high or higher than those generated by explosives or planar impact devices can be generated with a basic difference: the duration of the shock pulse is in the nanosecond range [8].

Fairand et al. [9] used these laser-induced shock pulses to modify the microstructure of engineering alloys, increasing their strength and fatigue resistance by what is commonly known as laser peening. Besides laser peening, shocks formed during laser irradiation have several other applications: densification of porous materials and spallation experiments [10], membrane disruption and stone fragmentation in biomedical applications [11], and propulsion of vehicles [12]. Modeling of the laser driven densification process has been attempted by Romain and Zagouri [13]. Laser driven shocks have also been utilized by Paisley et al. [14] and Labaste et al. [15] to drive flyer plates to study the dynamic behavior of materials.

More recently [16–19], pulsed X-ray diffraction has been used to obtain quantitative information of the lattice distortions at the shock front. These measurements can be used to resolve issues of dislocation generation and motion as well as lattice distortions at the shock front. Coupled with recovery experiments to examine the deformation substructures, laser shock experiments are being used to obtain an understanding of compressive shock defect generation and relaxation processes.

In this paper, recent work on the laser shock compression of copper and copper alloys is reviewed, examining the effects of crystallographic orientation, pressure decay, and stacking-fault energy on the deformation microstructure. There is specific emphasis on the slip to twinning

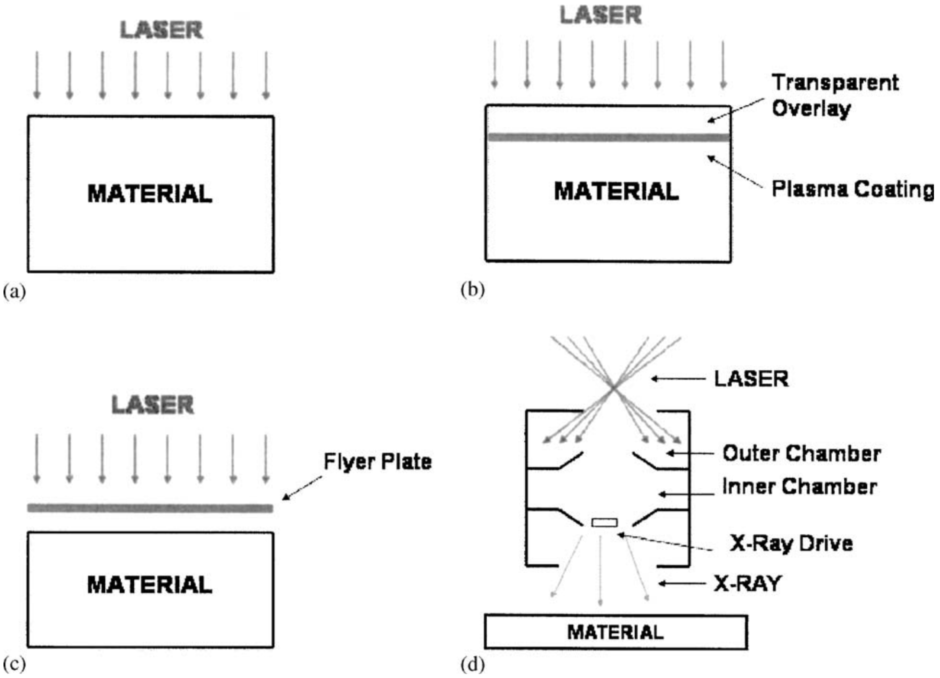

Fig. 1. (a) Laser incidence below the critical ablation threshold; (b) laser incidence as described by Anderholm [6] using a transparent overlay to increase achievable pressures (adapted from [8]); (c) laser driven shock developed by Paisely [14] and Labaste [15] to drive a flyer plate; (d) laser generated X-rays through a hohlraum (indirect drive).

transition. The formation of voids through the reflection of the shock pulse at the free surface is also examined.

2. Experimental techniques

Lasers deliver high amounts of energy in extremely short pulse durations enabling research in regimes of pressure and strain rates never before explored. Lasers typically produce less residual strain as compared to other techniques and post-shock heating is minimized because of the rapid quenching of the material due to the short pulses and specimen size/geometry. The shock experiments were carried out at the OMEGA Laser Facility at University of Rochester's Laboratory for Laser Energetics (LLE). Images of the facility are shown in Fig. 2(a)–(b). The input laser energies used in the experiments were 70, 200, and 300 J with a 2.5 ns pulse duration. The laser spot size was 3 mm. This experimental setup provided energy densities on the order of 50 MJ/m^2.

In situ dynamic X-ray diffraction experiments yield direct information of the change in the lattice as a shock wave propagates through a material [20]. X-rays are scattered from the atoms in different atomic planes and when these planes are compressed, the Bragg diffraction condition is met at a larger angle. The sample was probed by using X-rays generated by a high intensity beam impacting a thin metal foil as shown in Fig. 3. The diffracted X-rays from the crystalline lattice

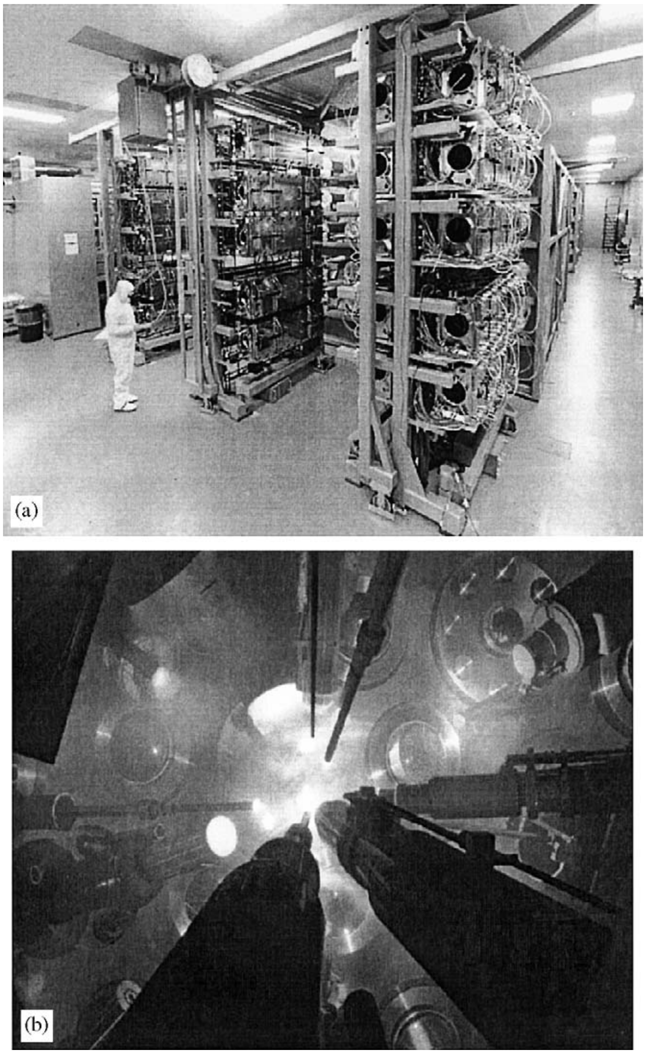

Fig. 2. Laser facility at the University of Rochester: (a) capacitor banks; (b) target chamber (used with permission).

planes were recorded on static film and X-ray streak cameras. Information on two different orientations can be recorded: parallel to the shock propagation direction and orthogonal to the shock direction. In copper oriented to [0 0 1], this corresponds to the (0 0 2) planes for parallel and (0 2 0) for orthogonal directions. Another measurement technique that has recently been developed is the use of a wide-angle detector where both static and compressed lattice planes can simultaneously be observed [21].

VISAR wave profile measurements were also performed during these experiments to obtain time-resolved data on the shock wave profile as it breaks from the free surface. Samples of various thicknesses were irradiated with different laser intensities to obtain the different release profiles. These provide a benchmark to understand the pressure decay effects observed in the recovered

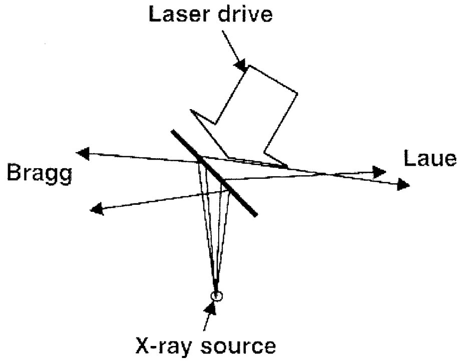

Fig. 3. Dynamic X-ray diffraction: sample set-up for shock compression and diffraction.

specimens. The results of the in situ dynamic X-ray diffraction and VISAR are reviewed herein and the complete results are described elsewhere [20].

For the recovery experiments, pure copper (99.999% pure) and copper–aluminum single crystals with orientations [0 0 1] and [$\bar{1}$ 3 4] were selected. The [0 0 1] orientation is highly symmetrical (eight primary slip systems) whereas [$\bar{1}$ 3 4] is highly asymmetrical (one primary slip system and two secondary slip systems). The [$\bar{1}$ 3 4] and [0 0 1] crystallographic orientations are marked in Fig. 4(a). Fig. 4(b) shows the stress–strain curves. The [$\bar{1}$ 3 4] orientation exhibits a delayed hardening due to the activation of a lower number of slip systems.

The samples were cut into cylinders with 3–5 mm length. They were mounted by press fit into foam-filled recovery tubes. The recovered cylinders were sectioned for TEM examination according to Fig. 5 by wire EDM and then mechanically ground to a thickness of 100 μm. The specimens (labeled A–E) were, after polishing, at distances of approximately 0.25, 0.75, 1.25, and 1.75 and 2.25 mm from the impact surface. Because the thin foils were prepared from samples cut at standard distances from the energy deposition surface, direct observation of changes in residual substructures could be correlated with decay of the laser pressure profile.

In order to determine the decay of shock hardening within the specimens, a Leco DM-400 machine was used. This provided microhardness values on the Vickers hardness scale which can be qualitatively compared to substructural observations. Loads of 25 or 50 gf for 15 s were used to make the indentations. The average microhardness for each value was determined from 10 to 15 hardness measurements. Two orientations were characterized: transverse sections similar to those prepared for TEM shown in Fig. 5 and longitudinal sections. The data from these measurements were compared with nanoidentation measurements. Nanoindentation was carried out in a Nano Instruments Nano II.

3. Results and discussion

3.1. Determination of shear strength under laser shock compression

A new technique for determining the strength of materials under extreme shock compression has been developed. It is presented by Meyers et al. [22] and will be reviewed here. It enables the

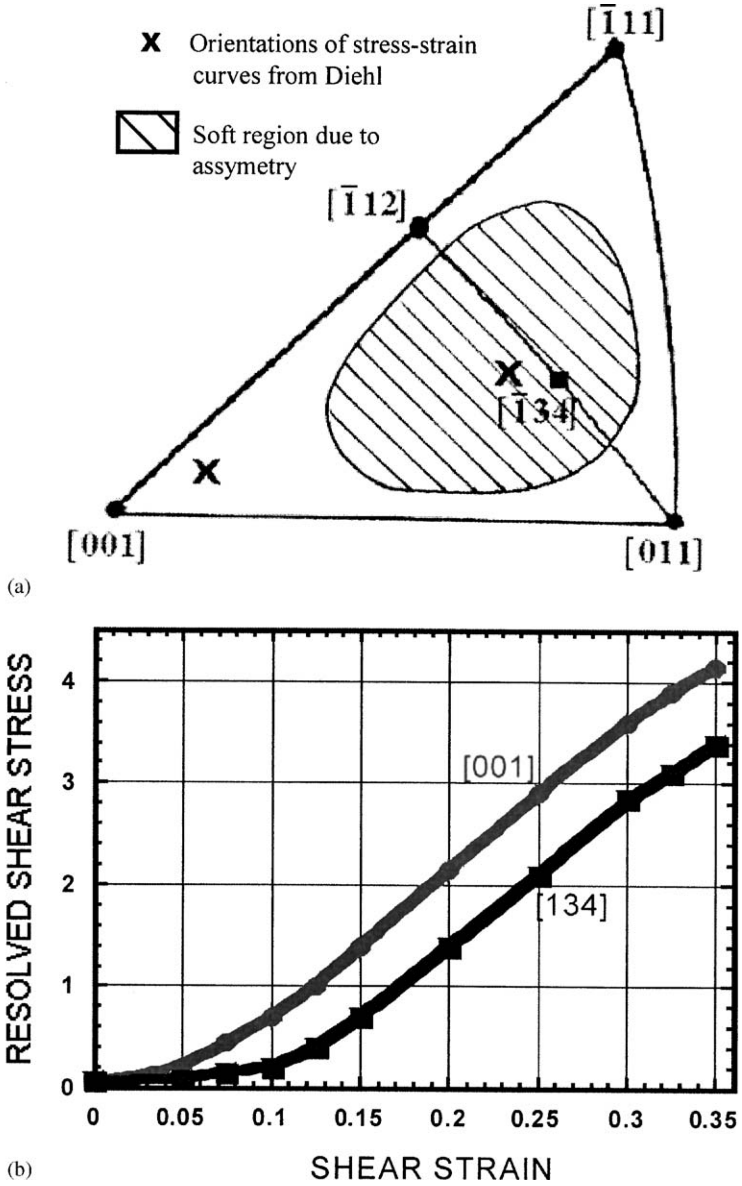

Fig. 4. (a) Standard stereographic projection showing [0 0 1] and $[\bar{1}\,3\,4]$ orientations, which were used in the laser-shock experiments. The asymmetric orientation $[\bar{1}\,3\,4]$ is 14° from [0 1 1] and 38° from [0 0 1]. (b) Stress–strain curves obtained from Diehl [1 1 4] for the [0 0 1] and $[\bar{1}\,3\,4]$ orientations.

establishment of the strength at a strain rate on the order of $10^7\,\mathrm{s}^{-1}$, which represents an increase in strain rate of at least one order of magnitude over results previously obtained. Fig. 6(a)–(d) shows a schematic arrangement of atomic planes during shock compression and the resultant distortions for different material responses. The [1 0 0] and [0 1 0] directions, perpendicular to (2 0 0) and (0 2 0), respectively, are represented. The (0 2 0) planes are diffracted in the Bragg

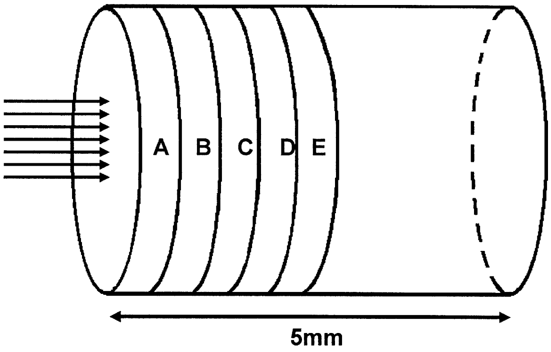

Fig. 5. Orientations characterized: transverse and longitudinal.

geometry (reflection); the incoming beam is incident on the surface opposite from the laser shock initiation. The (2 0 0) planes, that are parallel to the shock front, are imaged in the Laue geometry (transmission). If the distortion is purely elastic (Fig. 6(b)), the Laue diffraction does not show a change in angle, but the Bragg diffraction does. If there is totally hydrostatic compression, the Bragg and Laue angular changes are equal. This is shown schematically in Fig. 6(d). However, if the defects generated at or behind the front do not accommodate the distortion entirely, the (2 0 0) and (0 2 0) planes will exhibit different contractions. This was used [22] for calculating the strain parallel and perpendicular to the shock front. Diffraction measurements from these two perpendicular planes therefore enable the determination of the distortions at the shock front. Both time integrated and time-resolved measurements were made and are shown in Fig. 7. The results shown are for the calculated pressure of 18 GPa that corresponds to a V/V_0 ratio of 0.903 in pure copper. If one considers a hydrostatic compression, then one has [23]:

$$\left(\frac{a_s}{a_o}\right)^3 = \frac{V}{V_0} \tag{1}$$

where a_s and a_o are the lattice spacings in the shocked and original material, respectively. This situation is depicted in Fig. 6(d).

However, if there are residual stresses in the lattice, the compression is not completely hydrostatic and we have a situation such as the one seen in Fig. 6(c). The deviatoric elastic distortion of the lattice can be calculated purely from elasticity considerations. In Fig. 6(b), the shocked parameters a_{s1} and a_{s2} are shown ($a_{s2} < a_{s1}$). If ε_1 and ε_2 are the strains in the shock front plane and in a plane perpendicular to the shock plane (shock propagation direction), propagation direction, respectively, the shear strain can be expressed as

$$\gamma = \frac{\pi}{2} - \tan^{-1}\left(\frac{1+\varepsilon_1}{1+\varepsilon_2}\right). \tag{2}$$

For infinitesimal strains: $\gamma \approx \varepsilon_1 - \varepsilon_2$ and ε_1 and ε_2 are obtained by

$$\varepsilon_1 = \frac{a_{s1} - a_o}{a_o}, \quad \varepsilon_2 = \frac{a_{s2} - a_o}{a_o}. \tag{3}$$

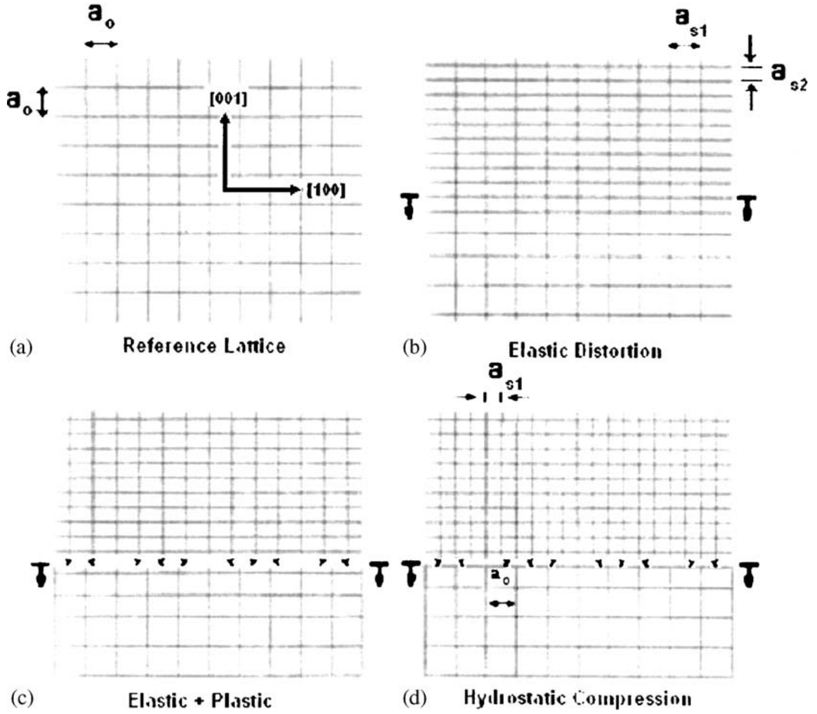

Fig. 6. Schematic representation of distortions caused in an ideal lattice oriented in an analous manner to shock experiments: (a) original configuration of planes; (b) elastic compression; (c) elastic + plastic compression with compression parallel to shock-front plane larger than perpendicular; (d) hydrostatic compression, when the compressions parallel and perpendicular are equal.

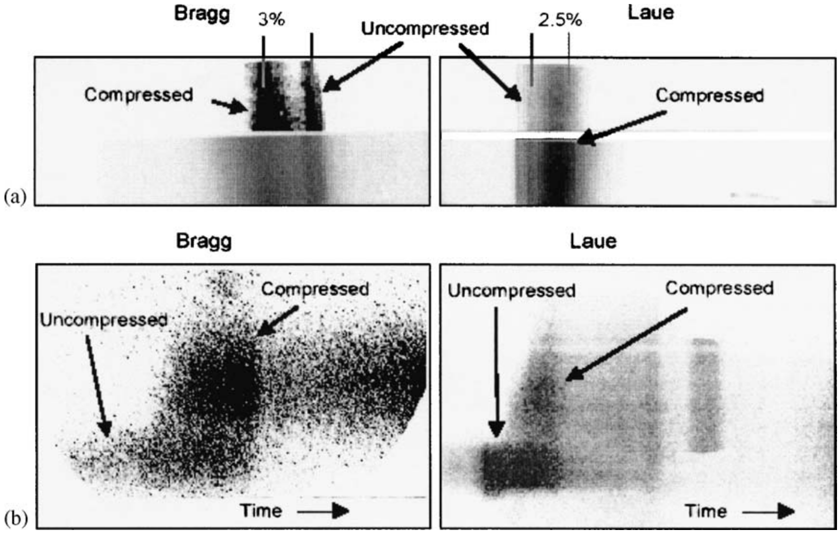

Fig. 7. Typical flash X-ray diffraction results for copper (2 0 0) and (0 2 0) planes, in Bragg (left) and Laue (right), respectively: (a) time-integrated data; (b) time-resolved data.

The values of a_s in the [1 0 0] and [0 0 1] directions are a_{s1} and a_{s2}, respectively (Fig. 6(b)). For the present case: $\varepsilon_1 = -0.025$ and $\varepsilon_2 = -0.034$.

The flow shear stress is given by

$$(\sigma_{12})_f = \gamma G. \tag{4}$$

The shear modulus of copper is 48.36 GPa. Hence,

$$(\sigma_{12})_f = (\varepsilon_1 - \varepsilon_2)G = 435\ \text{MPa}.$$

This value can be converted into an equivalent value for a grain size of 3 μm (the smallest size reported by Tong et al. [24]) by use of a Hall–Petch conversion. Using a Hall–Petch slope of $2.78 \times 10^{-4}\,\text{GPa}\,\text{m}^{-1/2}$ (from Zerilli and Armstrong [25]), one arrives at an additional stress of 45 MPa. Thus, the equivalent shear strength for a 3 μm specimen would be 485 MPa. The strain rate at the front is estimated from the strain divided by the rise time; t_f:

$$\dot{\varepsilon} = \frac{\varepsilon}{t_f} = \frac{2/3 \ln(V/V_0)}{t_f}. \tag{5}$$

For a pressure of 18 GPa: $V_0 = 0.9$. The pulse width can be estimated at a depth of 0.05 mm from the computed profile of Fig. 8 which corresponds to approximately the desired pressure. The estimated strain rate in shock compression [22] was $1.3 \times 10^7\,\text{s}^{-1}$. The results obtained herein are compared in Fig. 9 with high strain rate results by Follansbee and Gray [26] using a Kolsky–Hopkinson bar and Tong et al. [24] using a pressure-shear technique (Fig. 9). Tong et al. [24] had to use very thin (3 μm) specimens to reach their highest strain rates. The current result, obtained by flash X-ray diffraction, is consistent with an extrapolation from measurements made at lower strain rates. It is proposed that this technique has a wide range of applicability in exploring the strength of materials at strain rates heretofore unattainable.

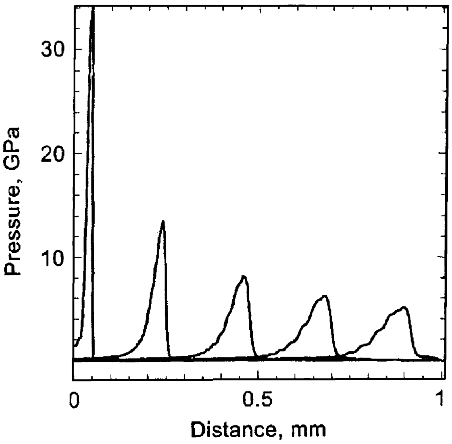

Fig. 8. Simulated pressure profiles as a function of distance from energy deposition surface for a laser impact energy of 70 J.

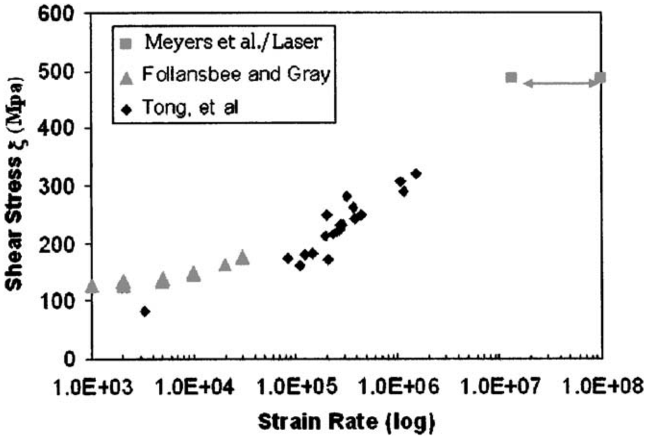

Fig. 9. Dependence of shear strength of copper on the strain rate; data by Tong et al. [24], Follansbee and Gray [26] and current estimates.

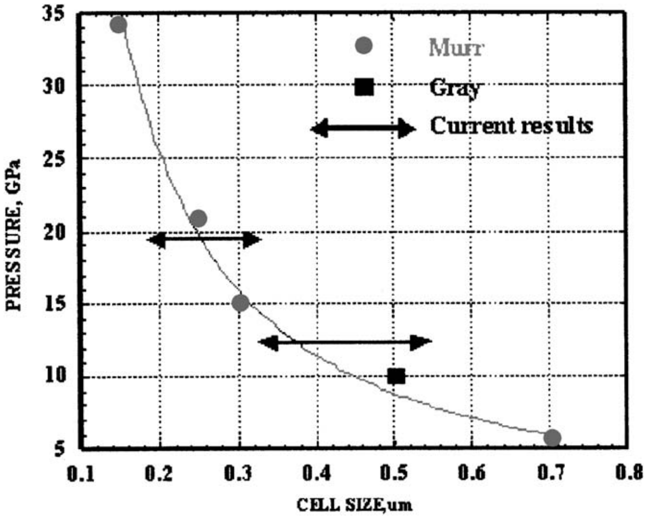

Fig. 10. Cell size as a function of pressure for shock loaded copper (adapted from Murr [28] and Gray [59]).

3.2. Recovery experiments: pressure decay and stacking fault energy effects

The stacking-fault energy in FCC metals plays an important role on the type of deformation observed under a given set of loading conditions. Deformation of metals results in systematic increases of dislocation densities, but the mechanism of this increase greatly depends on the stacking-fault energy. In FCC metals of medium to high stacking fault energy like aluminum, copper or nickel, cross-slip of partial dislocations is relatively easy. Low stacking fault-energy

FCC materials like gold and silver are hindered from cross-slip due to the difficulty in constricting the partials and therefore the dislocation density is increased by successive emission of dislocations and their motion along parallel planes.

3.2.1. TEM of pure copper

For the [0 0 1] orientation, shock experiments at 12 and 20 GPa pressures create a cellular organization with a medium density of $\frac{1}{2}$ [1 1 0]-type dislocations. The average cell size is between 0.2 and 0.3 μm cell size for 20 GPa. Qualitatively, these results confirm previous observations, albeit at a pulse duration that is lower by a factor of 10–100 than that applied by Murr [27]. Fig. 10 shows a plot of that data. The predicted cell size from Murr's data, at a pressure of 12 GPa, is 0.4 μm. One interesting feature is the observation of a large number of loops. For example, loops as small as 25 nm and as large as 250 nm are indicated in Fig. 11(a). Given the density of loops observed, far greater than that observed in undeformed Cu, it is reasonable to suggest that the loop nucleation is an essential event of the laser-induced shock compression. This is consistent with a mechanism of plastic deformation presented in [22] and schematically

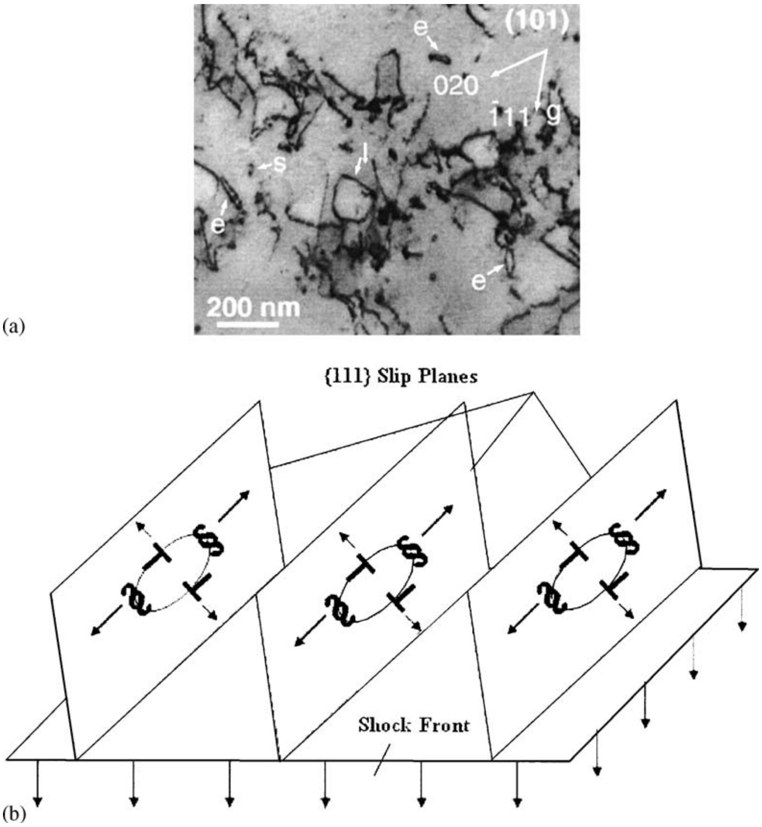

Fig. 11. (a) Observation of numerous loops in the 40 J shocked specimens. The different sizes (1 = large; s = small) and shapes (e = elongated) of the high density of loops are indicated in $B = [1\,0\,1]$. (b) Nucleation of dislocation loops at the shock front.

shown in Fig. 11(b). This mechanism for dislocation generation at the shock front, based on the nucleation of shear loops and their expansion behind the front, is still emerging. The predictions of dislocation density from this model compare favorably with measurements made over a range of shock compression pressures.

An energy input of 200 J (40 GPa initial pressure) created dense dislocation tangles and stacking faults. There are no readily discernible dislocation cells, but four variants of stacking faults are observed. These traces are analogous to previous observations by Murr [28]. The features are significantly different than the dislocation cells observed at the lower energy. These traces have orientations $\langle 2\,2\,0 \rangle$, as shown in Fig. 12.

Single crystal copper samples with $[\bar{1}\,3\,4]$ orientation were shocked at energies of 70 and 200 J corresponding to initial pressures of 20 and 40 GPa. The specimens shocked at 20 GPa contained a well-defined cellular network comprised of $\frac{1}{2}\langle 1\,1\,0 \rangle$ dislocations with a slightly larger (0.3–0.4 μm) average cell size, Fig. 13, as compared to the [0 0 1] orientation, Fig. 13. The dislocation density is on the order of $10^{13}\,\mathrm{m}^{-2}$. The cells are comprised primarily of three dislocation systems: $(1\,1\,1)\,[\bar{1}\,0\,1]$, $(1\,1\,1)\,[1\,\bar{1}\,0]$, $(\bar{1}\,1\,1)\,[1\,0\,1]$.

At the higher energy of 200 J for the $[\bar{1}\,3\,4]$ orientation, the deformation substructure continued to be cellular, albeit with a finer (0.15 μm) average cell size and a significantly higher dislocation density, $10^{14}\,\mathrm{m}^{-2}$, Fig. 14. This is in direct contrast to the mechanism change observed in [0 0 1]. Again, the three slip systems previously described dominate the deformation sub-structure. A large number of loops are also visible. These were found to contribute to the cell walls and were often commonly found within the cells.

The difference observed between the defect substructure of the [0 0 1] and $[\bar{1}\,3\,4]$ orientations is due to the orientation. Because of the symmetry of [0 0 1], interactions between dislocations are more common and enable the defects to relax into a stacking-fault-dominated substructure. The

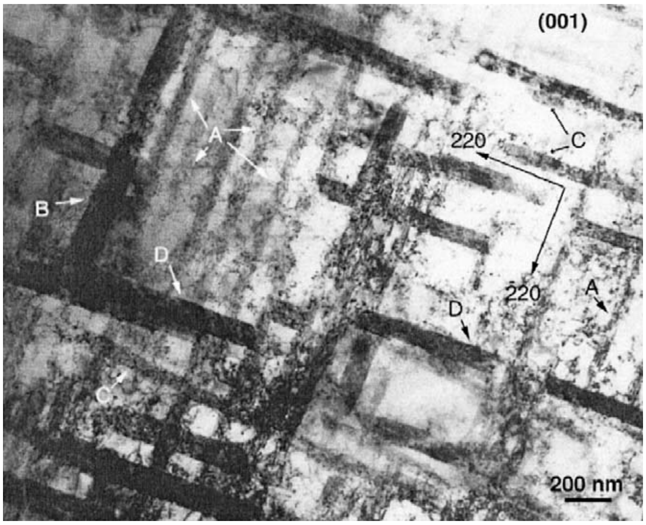

Fig. 12. Four sets of stacking faults (marked as A, B, C, D) are observed in [0 0 1] at 200 J (20 GPa): Variant A exhibits the highest density of occurrence, $g = 2\,0\,0$, $B = [0\,0\,1]$.

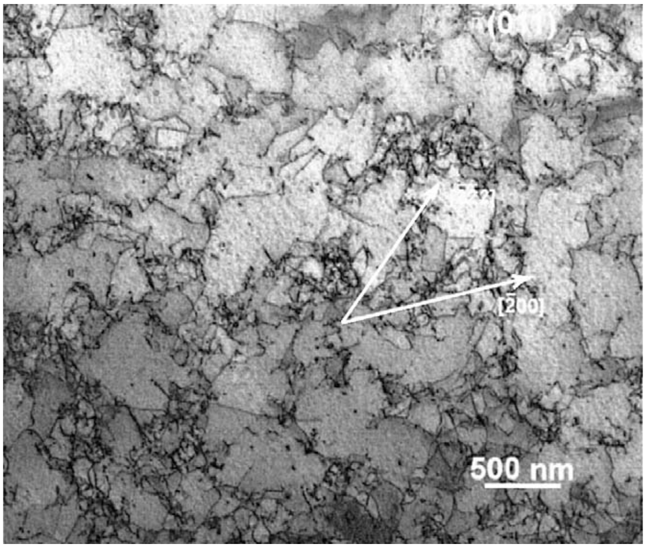

Fig. 13. Defect substructure of monocrystalline copper with orientation [$\bar{1}$ 3 4], shocked with a laser energy of 70 J in beam direction [0 1 1], $g = [\bar{2}\,\bar{2}\,2]$.

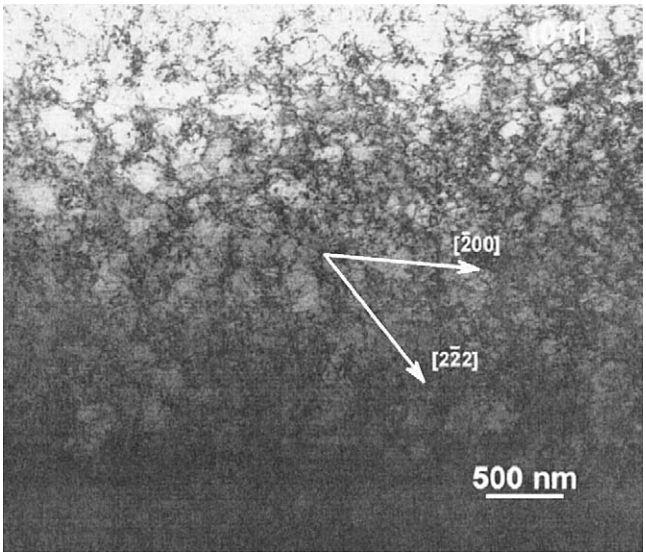

Fig. 14. Defect substructure of monocrystalline copper with orientation [$\bar{1}$ 3 4], shocked with a laser energy of 200 J in beam direction [0 1 1], $g = [\bar{2}\,\bar{2}\,2]$.

[$\bar{1}$ 3 4] orientation, consisting of dislocations with limited mobility and interaction, continues to form cells as the relaxed substructure to higher pressure levels.

3.2.2. Pressure decay effects in pure copper

The shock amplitude at the surface of the Cu crystal can be extracted from the laser impact energies and hydrocode calculations. This can be verified by VISAR measurements [20]. Due to

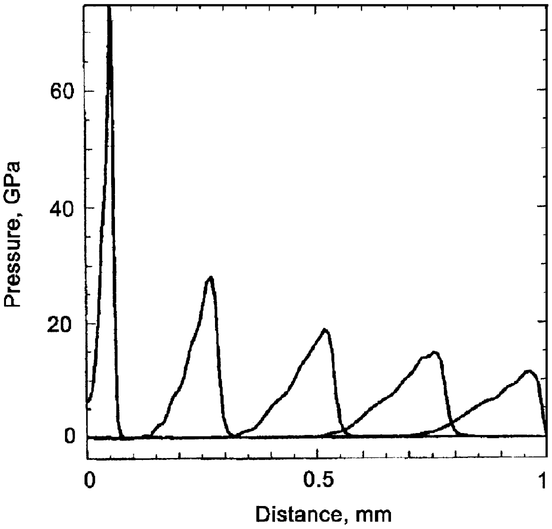

Fig. 15. Simulated pressure profiles as a function of distance from energy deposition surface for a laser impact energy of 200 J.

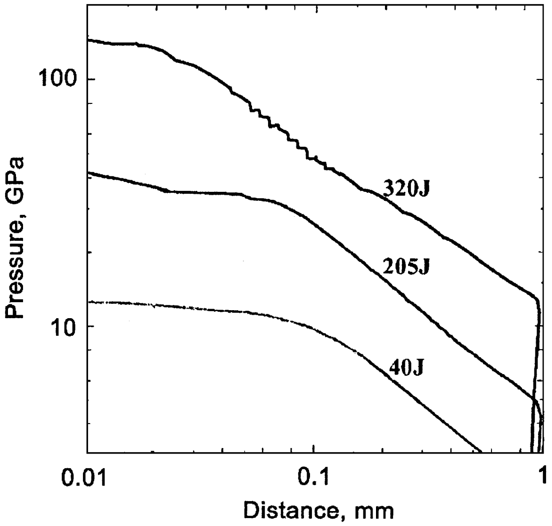

Fig. 16. Maximum pressure as function of distance from impacted surface for three shock impact energies.

the short duration of the shock created by the 3 ns laser pulse, the decay in the specimen is very rapid as shown by the calculated pressure profile plots. Snapshots of the pressure profiles at various times up to a depth of 1 mm are shown in Fig. 15 for the 200 J. The amplitude of the pressure wave in the sample decays substantially and the pulse duration broadens as a function of distance. Fig. 16 shows the decay of the maximum pressure in the specimens at these three energy levels.

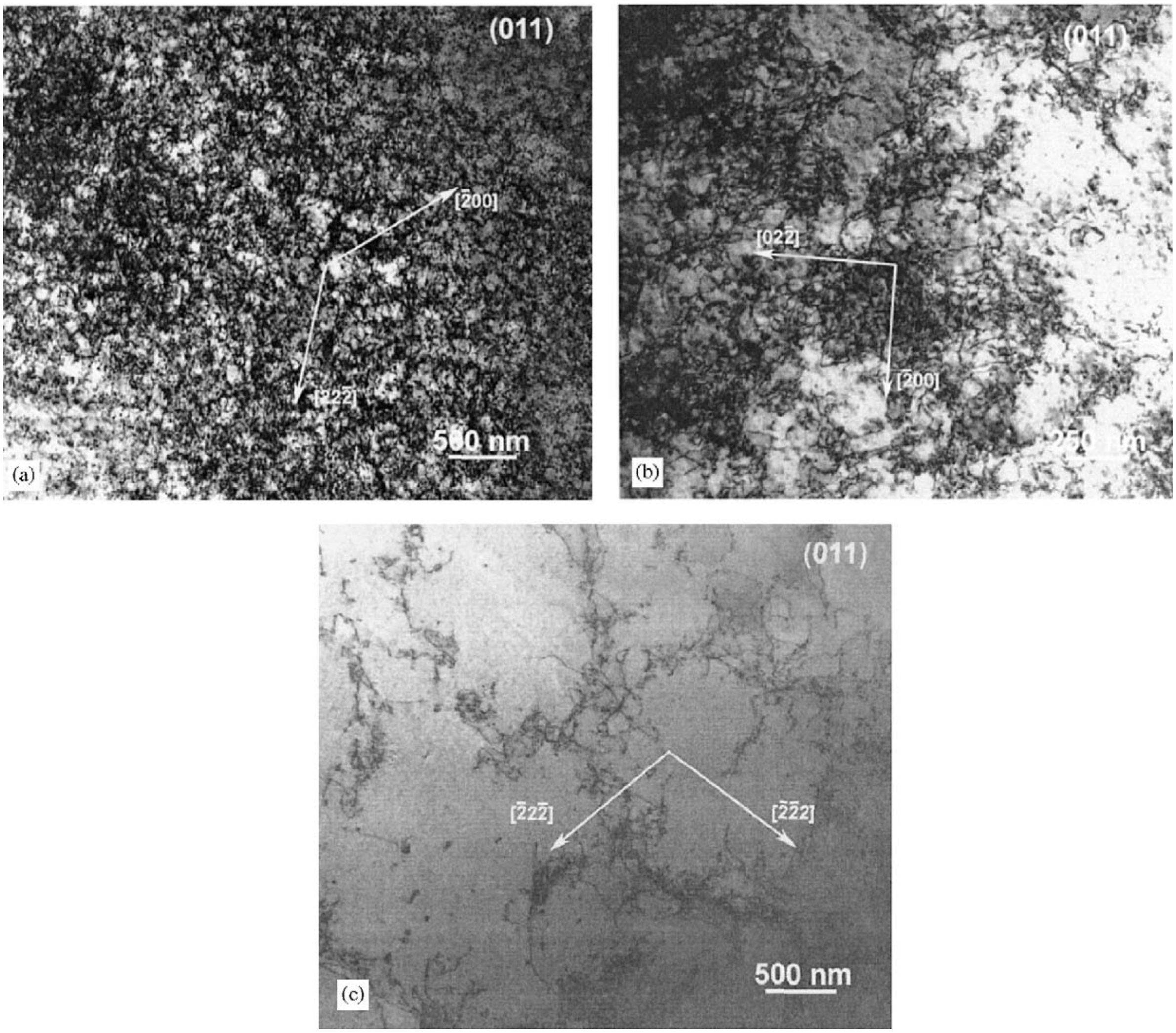

Fig. 17. TEM images of the defect substructures showing the pressure decay effects of $[\bar{1}\,3\,4]$ Cu at different distances from the laser impact surface shocked at 200 J (for each image, beam direction $B = [0\,1\,1]$): (a) 0.25 mm, $g = [2\,2\,\bar{2}]$ (b) 1.25 mm, $g = [0\,2\,\bar{2}]$; (c) 2.25 mm, $g = [\bar{2}\,2\,\bar{2}]$.

Fig. 17(a)–(c) show the dislocation cells for the 40 GPa (200 J) at 3 locations: A, C and E. The decay in pressure, shown in Fig. 8, is accompanied as expected by an increase in cell size and decrease in dislocation density. The average cell sizes are: 0.14 μm for specimen A (Fig. 17(a)); 0.22 μm for specimen B (not shown); 0.41 μm for specimen C (Fig. 17(b)), 0.76 μm for specimen D (not shown), and 1.43 μm for specimen E (Fig. 17(c)). The dislocation densities decrease from $10^{14}\,\mathrm{m}^{-2}$ at the front to $10^{11}\,\mathrm{m}^{-2}$ at position E.

In Fig. 18(a), the cell sizes as a function of distance from the laser irradiated surface are plotted for the three energies. The cell sizes vary consistently with the three energy levels. Fig. 18(b) shows that the cell size and pressure correlate at different locations within the specimen.

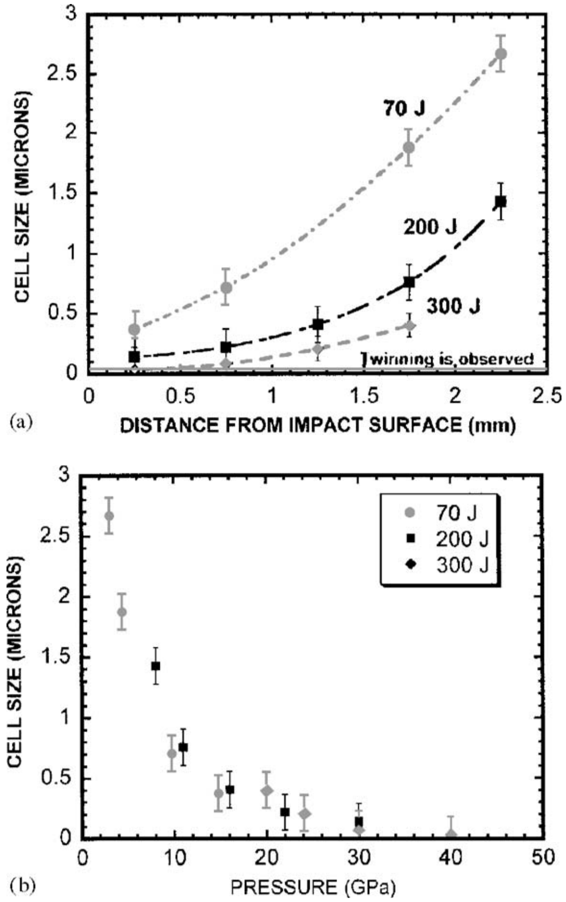

Fig. 18. (a) Cell size as a function of distance from the impact surface for the [$\bar{1}$ 3 4] crystal orientation at three initial energies: 70, 200, and 300 J. Twinning is observed when dislocation cell sizes fall below an average size of 0.05 μm represented by the bottom line; (b) Cell size as a function of estimated pressure for the three energy levels.

3.2.3. *Copper–aluminum alloys*

As previously mentioned, the addition of small amounts of aluminum (<7 wt%, the solubility limit) lowers the stacking-fault energy (SFE) of copper. Early work by Johari and Thomas [29] demonstrated this effect on the defect substructure in copper aluminum alloys. In this section, a detailed analysis of the effect of stacking-fault energy on the threshold pressure for twinning is presented. Systematic differences were observed by transmission electron microscopy in the deformation substructures of the different compositions: copper–2 wt% aluminum (4.2 at%) and copper–6 wt% aluminum (12.6 at%). The experimentally obtained stacking-fault energies of the Cu–2 wt% Al and (Cu–6 wt% Al) are 37 and 5 mJ/m^2, respectively.

Both pressure and crystal orientation significantly affected the deformation substructures of laser shocked Cu–2 wt% Al. The samples with [0 0 1] orientation shocked at 70 J (20 GPa initial pressure) had regular cells with an average size of 250 nm and cell wall thickness of 50 nm. The average disolocation line length was considerably longer, 150 nm, and the dislocation density was

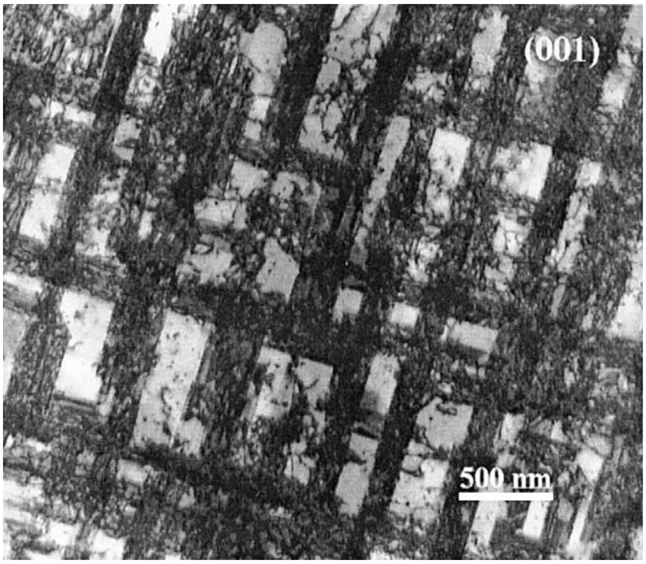

Fig. 19. Bright field images of Cu–2 wt% Al with [0 0 1] orientation shocked at 200 J (40 GPa) imaged with $B = (0\,0\,1)$ and $g = [0\,2\,0]$ for all conditions: Specimen A ~0.25 mm from impacted surface.

on the order of $10^{14}\,\mathrm{m}^{-2}$. The dislocations were also observed to gather on the primary planes. The dislocation substructure for this condition (70 J) was made of the eight primary slip systems.

In the Cu–2 wt% Al with [0 0 1] orientation and shocked at 200 J, stacking faults were readily observed as the dominant defect substructure, Fig. 19. Because of the 2 wt% addition of aluminum, the stacking-fault energy is nearly half that of pure copper, and one would expect to observe twinning. However, this is not the case. Instead, four stacking-fault variants are observed. These stacking faults are similar to those observed for pure copper (Fig. 20(a)–(c)). The faults are well defined with clean boundaries having a regular spacing of 250 nm.

The Cu–2%wt Al with $[\bar{1}\,3\,4]$ orientation was observed to have a substantially different defect substructure than pure copper or Cu–2%wt Al with [0 0 1] orientation. The effects of the change in stacking-fault energy were generally more pronounced. The dislocations were arranged in planar arrays. The defect substructure consisted of long dislocation lines as shown in Fig. 21. The dislocation line length averaged 500 nm and the dislocation density was $10^{13}\,\mathrm{m}^{-2}$. It is obvious that at this condition there is one dominant slip system $[\bar{1}\,0\,1]$ (1 1 1); the two secondary systems are also observed, but in less proportions. A number of dislocation loops are also observed.

Cu–2%wt Al with $[\bar{1}\,3\,4]$ orientation shocked at 200 J exhibited twinning (position A, Fig. 22). Two variants are observed. It appears that the domain of the larger twin may be the nucleation site for the second twin. The twins were found in a relatively low proportion, but are the systems predicted by Schmid factor calculations. The twins varied in size and proportion with the primary variant, (1 1 1) $[\bar{2}\,1\,1]$, having an average length of 4 μm and a width of 20–30 nm. The secondary variant, $[1\,\bar{1}\,1]$ $[\bar{1}\,\bar{1}\,\bar{2}]$, was greater in number, but shorter in length with an average of 2 μm. It was expected that a co-secondary twinning variant would also be found, $(1\,\bar{1}\,1)$ $[1\,\bar{1}\,\bar{2}]$, but the occurrence of this system was relatively rare. This suggests that the sample may have been slightly misaligned from the $[\bar{1}\,3\,4]$ loading axis, and thereby preferred the two observed twinning systems

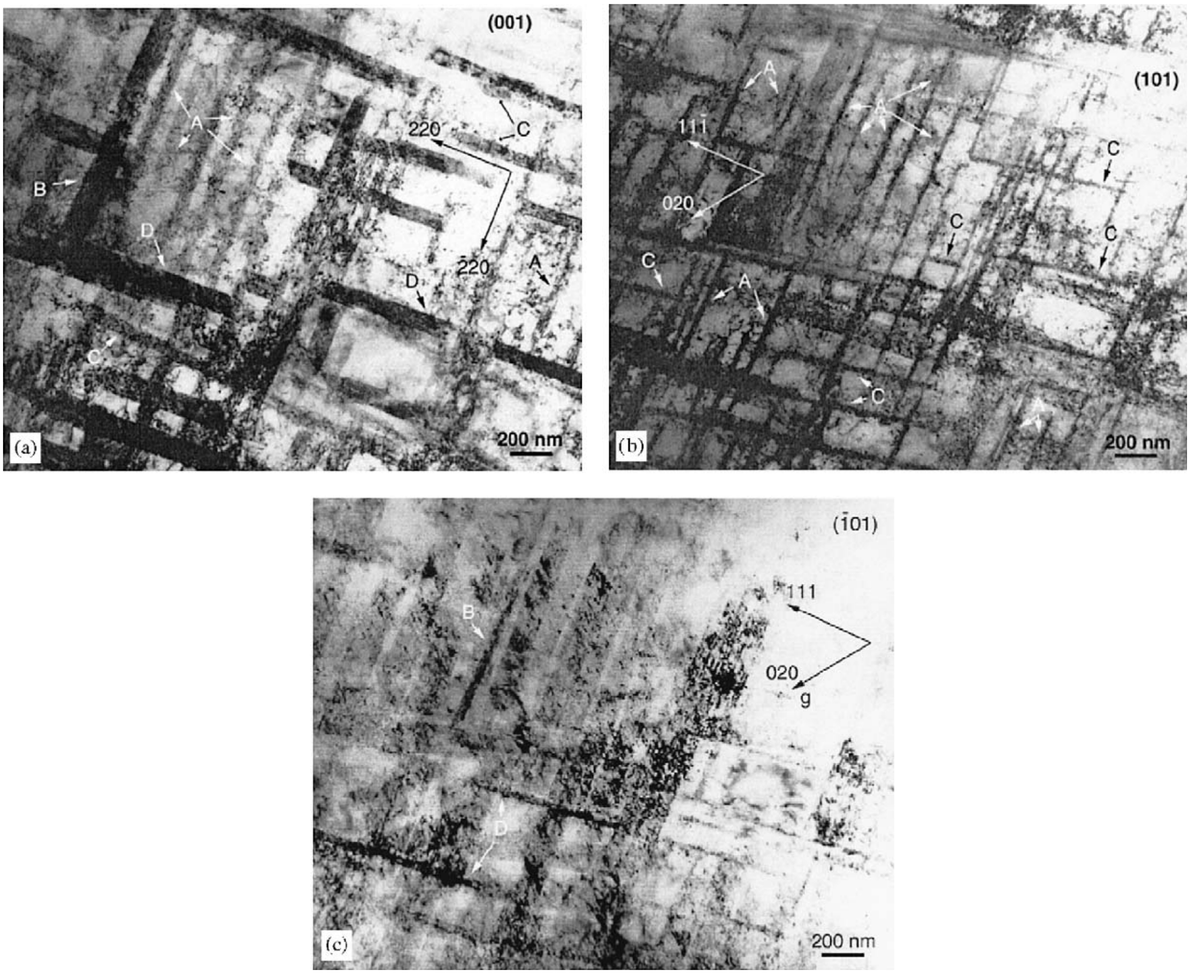

Fig. 20. Four sets of stacking faults (marked as A, B, C, D) are observed in [0 0 1] at 200 J (20 GPa): (a) Variant A exhibits the highest density of occurrence, $g = 2\,0\,0$, $B = [0\,0\,1]$; (b) Stacking fault variant A imaged in the near edge orientation, $g = 0\,2\,0$; $B = [0\,0\,1]$; (c) Stacking fault variants C and D observed in the near edge orientation, $g = 0\,2\,0$, $B = [\bar{1}\,1\,1]$.

having higher Schmid factors than calculations indicate. A high density of dislocations was also observed (not shown here).

The defect substructure for all energies in Cu–6 wt% Al with [0 0 1] orientation consisted of either stacking faults or dislocations since, for this system, the stacking-fault energy is less than 5 mJ/m^2. The dislocation structure consists of large planar arrays and regions of dislocation pileup since the low stacking-fault energy inhibits cross-slip. Many of the dislocations observed were Shockley partials: $\{1\,1\,\bar{1}\}\ 1/6\ \langle 1\,1\,2\rangle$. The defect substructure was primarily made up of planar arrays of dislocations and had a dislocation density on the order of $10^{13}\,\mathrm{m}^{-2}$ and a line length of 500 nm. The planar arrays were spaced at a distance of 1 μm. Stacking faults and stacking-fault

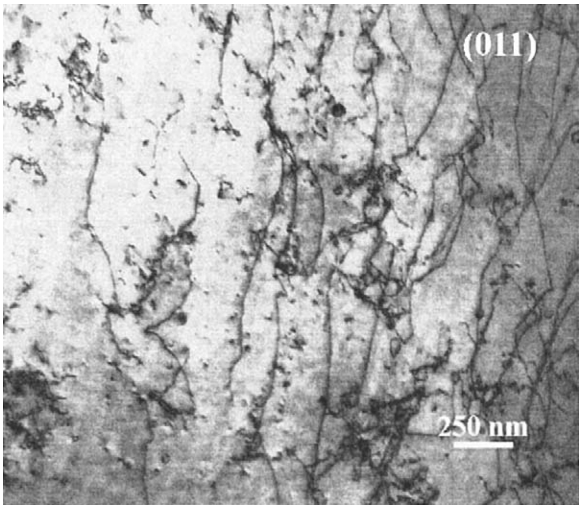

Fig. 21. Bright field images of Cu–2 wt% Al with $[\bar{1}\,3\,4]$ orientation shocked at 70 J (20 GPa) imaged with $B=(0\,1\,1)$ and $g=[0\;2\;\bar{2}]$ for all conditions: Specimen $B{\sim}0.75$ mm from impacted surface.

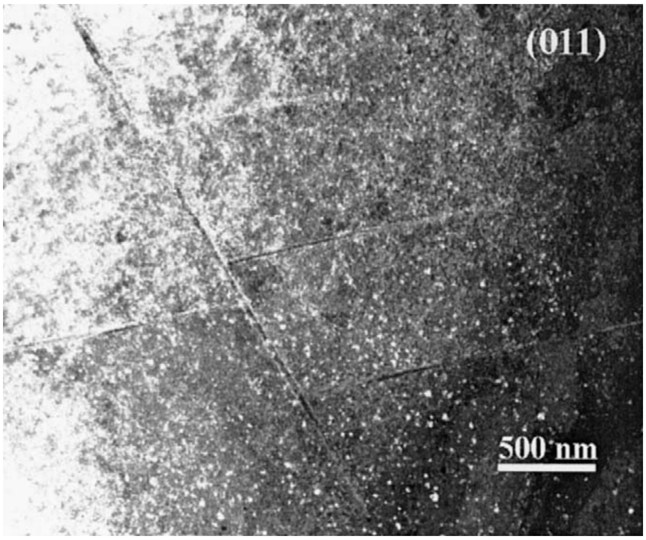

Fig. 22. Bright field images of Cu–2 wt% Al with $[\bar{1}\,3\,4]$ orientation shocked at 200 J (40 GPa) imaged with $B=(0\,1\,1)$ and $g=[0\;2\;\bar{2}]$ for all conditions: Specimen $A{\sim}0.25$ mm from impacted surface.

tetrahedra were also observed. The fault spacing was equivalent to the distance between planar arrays (1 μm).

For the Cu–6 wt% Al with [0 0 1] orientation and laser shocked at 200 J, the defect substructure was predominantly stacking faults (Fig. 23(a)–(c)). The stacking faults had a width of 100 nm,

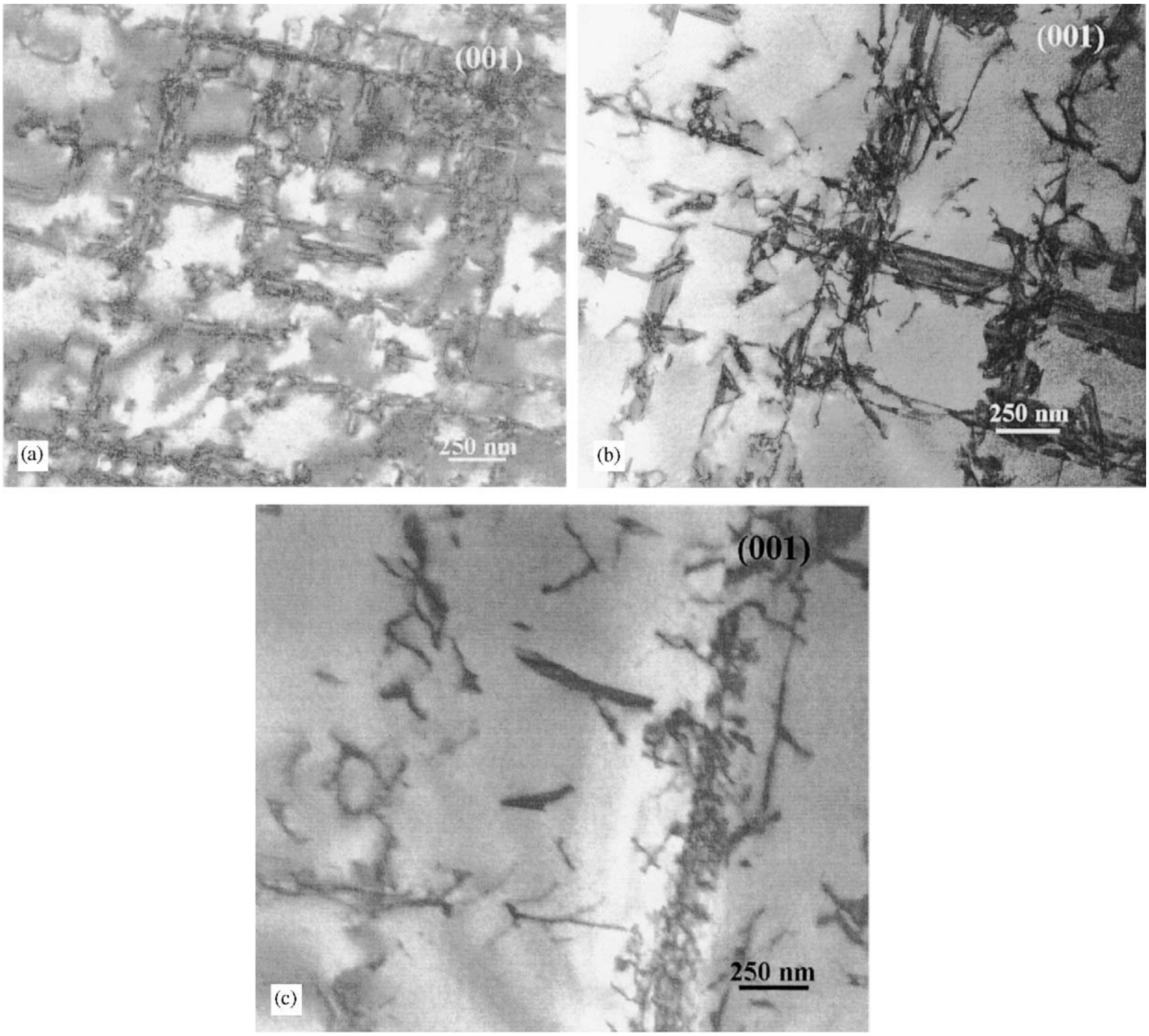

Fig. 23. Bright field images of Cu–6 wt% Al with [0 0 1] orientation shocked at 200 J (40 GPa) imaged with $B = (0\,0\,1)$ and $g = [0\,2\,0]$ for all conditions: (a) Specimen A~0.25 mm from shocked surface; (b) Specimen B~0.75 mm from shocked surface, (c) Specimen C~1.25 mm from shocked surface.

length of 1 μm, and spacing of 400 nm. The areal density was $0.84 \times 10^5\,\mathrm{m}^{-1}$. Dislocations were also observed throughout the specimen, typically near the fault boundaries.

For the $[\bar{1}\,3\,4]$ orientation of the Cu–6 wt% Al, three variants of stacking faults were observed in the 70 J condition with one system preferred. Dislocations were also observed. The stacking fault width was 250 nm on average and the spacing 300 nm. The areal density was on the order of $0.1 \times 10^5\,\mathrm{m}^{-1}$. Dislocations were arranged in planar arrays and tangles with a density of $10^{13}\,\mathrm{m}^{-2}$. The dislocation line length and planar spacing was about 1 μm and 250 nm, respectively.

The Cu–6 wt% Al $[\bar{1}\,3\,4]$ specimens shocked at 200 J contained a residual defect substructure similar to the 70 J specimens. Partial dislocations dominate the defect substructure. It had a dislocation density of $10^{13}\,\mathrm{m}^{-2}$ and an average line length of nearly 1 μm. The dislocations are preferentially aligned along specific planes with a spacing of 1 μm and it is evident that there is one primary slip system, $[\bar{1}\,0\,1]$ $(1\,1\,1)$. Some stacking faults were also observed with most being aligned to $[\bar{2}\,1\,1]$ $(1\,1\,1)$.

It was found that stacking faults typically formed at high pressures and then were found to decay into either cells or planar arrays of dislocations as the pressure decayed through the sample. As expected, decreasing stacking-fault energy enhanced the propensity to form stacking faults for both orientations. Similarly, cells and planar arrays became more clearly defined as the pressure decreased and pulse duration increased. Twinning was not readily observed in most of these conditions suggesting there may be some unresolved time dependence to nucleate twins. However, it is also possible that many of the stacking faults observed are actually nano-twins as the thickness of the twin could be small and therefore traditional transmission microscopy methods may be unable to resolve the changes in the structure.

The experimental results are plotted in Fig. 24(a)–(c). The positions A–D were converted into pressures through the computational calculations. The transition from loose dislocations/cells to stacking faults/twins is approximately indicated in Fig. 24(a). Fig. 24(b) and (c) show the change of dislocation densities and stacking fault densities versus pressure, respectively. The energetics in loop nucleation for perfect and partial dislocations is discussed in a later section. Both deformation twinning and stacking fault energy formation are the direct consequence of partial dislocation loop nucleation and expansion. In the case of twinning, one has separated and prescribed arrays of partial dislocation loops on adjacent planes.

3.3. Microindentation and nanoindentation hardness measurements

It is well established that shock compression strengthens ductile materials more effectively than quasi-static deformation at the same effective strains. This hardening effect has been attributed to increased dislocation densities formed (and stored thereafter) in shock compression. The flow stress is related to the dislocation density by

$$\tau = \tau_0 + k\rho^{1/2} \tag{6}$$

where τ is the shear stress, τ_0 is the stress obtained when $\rho^{1/2}$ is extrapolated to zero, k is a material constant, and ρ is the dislocation density. Additionally, shock loading can increase the density of twinning, stacking faults, and point defects which are reflected in the hardness and strength of the recovered material. In this study, hardness measurements were made on the specimens characterized by transmission electron microscopy using micro- and nanoindentation measurements. These methods provided an excellent way to examine the deformation substructures and relate the TEM observation images to actual mechanical properties.

Fig. 25(a) and (b) show the changes in hardness using microindentation hardness measurements for the Cu–2 wt% Al. The hardness increases substantially with increasing laser shock energy; a rapid decrease in the hardness is observed after the first 1 mm of material. This is entirely consistent with cell size measurements shown in Fig. 18.

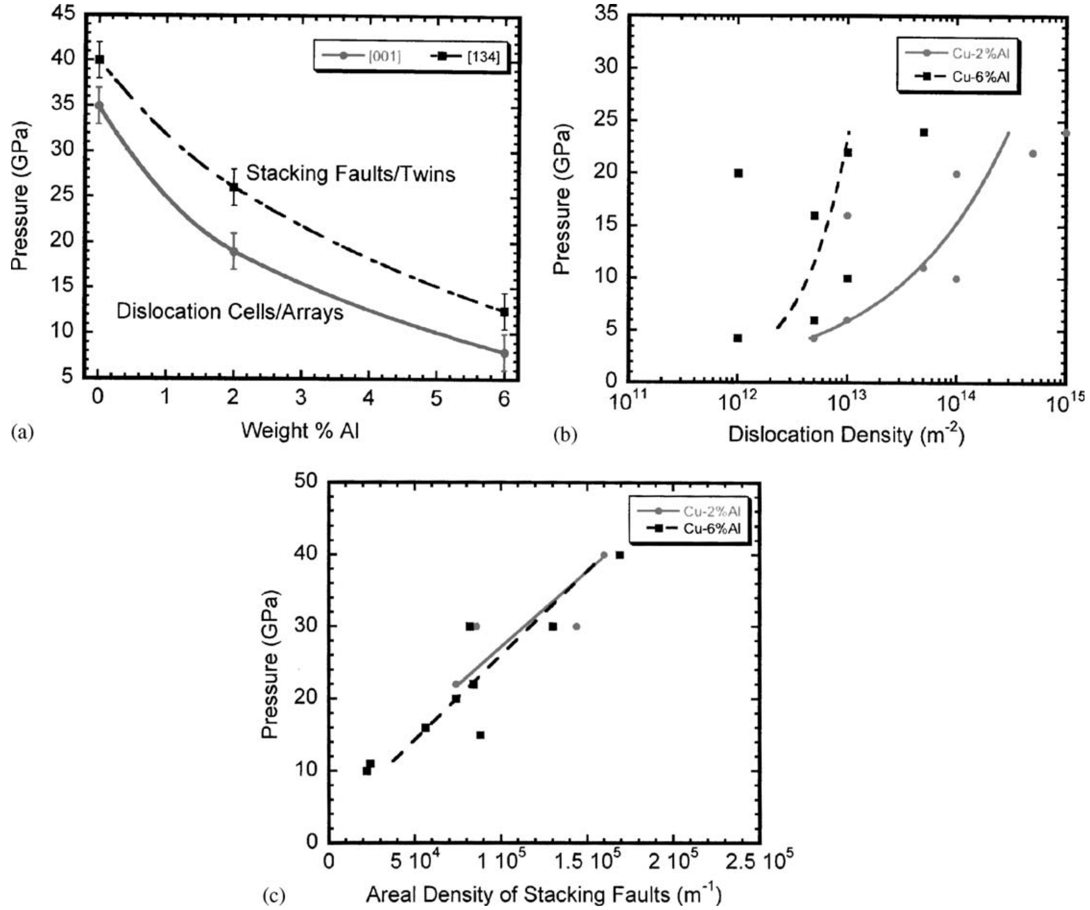

Fig. 24. Experimental results for laser-shocked Cu–Al alloys: (a) Experimentally observed transition from dislocation cells and planar arrays to stacking faults and twins as a function of composition; (b) experimentally observed dislocation densities as a function of pressure; (c) experimentally determined areal densities of stacking faults as a function of pressure.

3.4. The slip-twinning transition in Cu and Cu–Al alloys

In shock loading, the dislocation arrangements are more uniform than after quasi-static deformation of the material. High stacking-fault energy materials often are found to twin at a threshold pressure during shock compression whereas they may never twin at quasi-static conditions except at very low temperatures. Twinning propensity, however, increases in both modes of deformation (quasi-static and high-strain rate) when the stacking fault energy is decreased. Stacking-fault energy can be manipulated in materials by alloying. For example, in copper, which has a relatively high stacking fault energy (78 ergs/cm^2 [30]), the stacking fault energy is nearly cut in half by adding 2 wt% aluminum. This effect can be correlated to the change in the electron to atom ratio (e/a) in an alloy as given be (2.4)

$$e/a = (1-x)Z_1 + Z_2 = 1 + x\,\mathrm{d}Z, \tag{7}$$

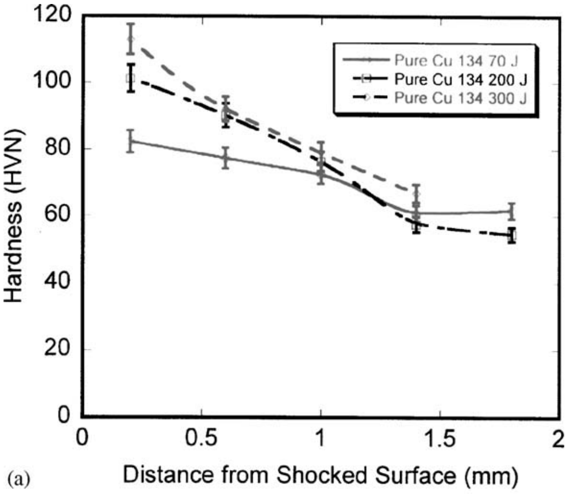

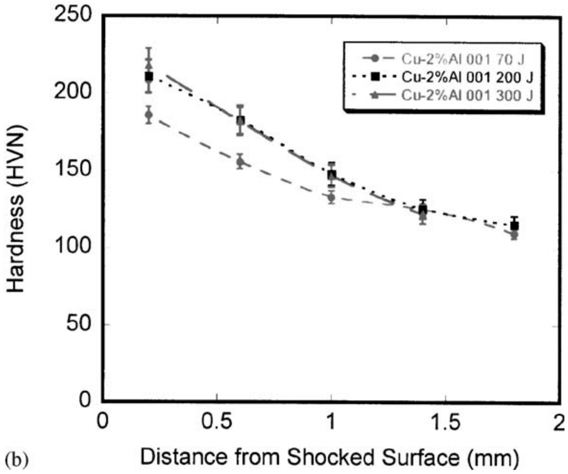

Fig. 25. Microhardness measurements taken on transverse sections (A, B, C, D) as a function of distance from impact surface (0.25, 0.75, 1.25, and 1.75 mm): (a) pure copper with $[\bar{1}\,3\,4]$ orientation; (b) Cu–2wt% Al with [0 0 1] orientation.

where x is the atomic fraction of the solute in the alloy, Z_1 and Z_2 are the number of valence electrons for the solute and solvent atoms, respectively, and $\mathrm{d}Z$ equals (Z_1-Z_2) [31].

It was shown by Thomas [32] that slip and twinning are competing deformation mechanisms and that they have a profound effect on the mechanical properties of materials such as martensitic steels and FCC metals. Slip has much higher temperature dependence than twinning. This leads to separate slip and twinning domains. The goal of the current research effort has been to develop a constitutive description to quantitatively describe this transition as a function of orientation, stacking-fault energy, temperature, grain size, and strain rate.

The methodology to be used in the prediction of the threshold shock amplitude for twinning was delineated by Murr et al. [33] and Meyers et al. [22,34]. The procedure presented herein can be used to predict the critical pressure for twinning in shock compression experiments. Different metals have different threshold pressures for the initiation of twinning. It has been established by Murr [28] and Johari and Thomas [29] that this pressure is a function of stacking-fault energy, for FCC metals. Another important factor is orientation, which has never been quantified except in terms of resolved shear stress, which does not adequately describe the differences.

This is corroborated by experimental evidence presented earlier. It is assumed that at the threshold pressure:

$$\sigma_\mathrm{T} = \sigma_\mathrm{S}. \tag{8}$$

One can obtain the critical twinning pressure as a function of ε, $\dot{\varepsilon}$, and T. The application of this criterion to the shock front necessitates the knowledge of the strain rate. The strain rate at the shock front has been established by Swegle and Grady [35] to be

$$P = k_\mathrm{SG}\dot{\varepsilon}^{1/4}. \tag{9}$$

Two separate aspects have to be considered in the analysis: (a) shock heating and (b) plastic strain at the shock front. Both shock heating and plastic strain by slip (and associated work hardening) alter the flow stress of material by slip processes and need to be incorporated into the computation. The total (elastic + plastic) uniaxial strain, ε, at the shock front is related to the change in specific volume by:

$$\frac{V}{V_0} = e^{\varepsilon}. \tag{10}$$

The pressure can be expressed as a function of strain from the shock conservation equation and Eq. (10):

$$P = \frac{C_0^2(1 - e^{\varepsilon})}{V_0[1 - S(1 - e^{\varepsilon})]^2}. \tag{11}$$

The constitutive response of the copper monocrystal is represented by the modified MTS expression below:

$$\sigma = \sigma_0 f(\varepsilon)\left[1 - \left(\frac{kT}{Gb^3 g_0}\ln\left(\frac{\dot{\varepsilon}_0}{\dot{\varepsilon}}\right)\right)^{2/3}\right]^2. \tag{12}$$

The thermal and strain-rate parameters p, q, g_0, and $\dot{\varepsilon}_0$ are taken from Follansbee and Gray [26] and Follansbee [36]. The given values are $p = \frac{1}{2}$, $q = \frac{3}{2}$, $g_0 = 0.8$, and $\dot{\varepsilon}_0 = 10^{-4}\ \mathrm{s}^{-1}$. The work hardening $f(\varepsilon)$ was incorporated by taking a polynomial representation of the stress–strain curve for single crystals with the [0 0 1] and [$\bar{1}$ 3 4] orientations as shown in Fig. 4 [57]. This is the only manner by which a three stage response can be incorporated without excessive complexity. The [0 0 1] orientation is expected to have the lowest threshold pressure for twinning of all orientations, whereas [$\bar{1}$ 3 4] should have a substantially higher threshold pressure due to its more gradual hardening. The polynomial used in these calculations is, for [0 0 1]:

$$f(\varepsilon) = 45510\varepsilon^6 - 86899\varepsilon^5 + 63406\varepsilon^4 - 21834\varepsilon^3 + 2901.8\varepsilon^2 + 464.8\varepsilon^1 - 1.92. \tag{13a}$$

For [$\bar{1}$ 3 4]:

$$f(\varepsilon) = -10871\varepsilon^6 + 1431\varepsilon^5 - 7329\varepsilon^4 + 16903\varepsilon^3 + 1268\varepsilon^2 - 2.34\varepsilon^1 + 0.07. \tag{13b}$$

The normal twinning stress (σ_T) used in this calculation was 490 MPa [37] for pure copper. Eqs. (13a) or (13b) are inserted into Eq. (12), and Eq. (8) is inserted into Eq. (12). Application of Eq. (8) leads to the threshold stress at a low value of the plastic strain. This provides a first estimate of the pressure, P. This pressure is then used to recalculate the shock strain and temperature. These values are then fed back into Eqs. (9) and (12), and a second pressure is calculated. This iterative process converges to the critical twinning pressure.

3.4.1. Solid solution strengthening

The addition of small amounts of aluminum to copper not only lowers the stacking fault energy, but drastically influences the strength and hardness. In pure metals, dislocations are relatively mobile, but when solute atoms are added the dislocation mobility is greatly reduced. In these alloys, the solute atoms become barriers to dislocation motion and can have the effect of locking them. Substantial work has been done developing solid solution theory for concentrated solid solutions [38–41]. It has been determined that the flow stress of concentrated solid solutions is related to the atomic concentration of the solute by:

$$\sigma_0 \propto [C_S]^{2/3}, \tag{14}$$

where σ_0 is the flow stress and C_S is the concentration of the solute. Copper–aluminum has been shown to exhibit this dependence [42]. It was therefore assumed reasonable to incorporate this compositional term into the modified MTS equation as shown below.

$$\sigma = \sigma_0 (C_S)^{2/3} f(\varepsilon) \left[1 - \left(\frac{kT}{Gb^3 g_0} \ln\left(\frac{\dot{\varepsilon}_0}{\dot{\varepsilon}} \right) \right)^{2/3} \right]^2 . \tag{15}$$

The effect of stacking-fault energy was also incorporated into twinning stress. With modified Eqs. (8) and (15), it is possible to calculate the critical pressure for twinning in copper–aluminum alloys. Fig. 26 shows the results from this analysis. For copper–aluminum with [0 0 1] orientation, the critical pressure necessary to nucleate twinning drops from 16 GPa (for pure copper) to 2.5 GPa (for Cu–6 wt% Al). For copper–aluminum oriented to [$\bar{1}$ 3 4], the change is from 25 GPa (for pure copper) to 5 GPa (for Cu–6 wt% Al). The results for pure copper are reasonable when compared to the results obtained by DeAngelis and Cohen [58]. They found copper oriented to [0 0 1] and [1 1 1] to twin at pressures above 14 and 16 GPa, respectively.

3.5. Incipient spallation and void growth

The study of the nucleation and growth of voids in ductile metals is of significant interest for the understanding of failure under overall tensile loading. Such failure, for example, can occur upon reflection of tensile waves from a free surface of the shock-compressed plate. Material failure by void growth under dynamic loading conditions leads to spalling. Extensive analytical and computational research has been devoted to analyze ductile void growth and coalescence in various materials and under various loading conditions.

This section describes an alternative mechanism of void growth by dislocation emission from the surface of the void. It will be analytically shown, for a two-dimensional configuration, that the imposed stresses in the laser shock experiments are sufficient for emitting dislocations from the

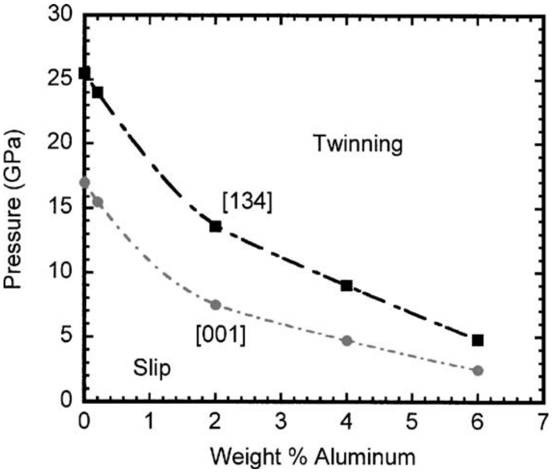

Fig. 26. Calculated effect of composition (SFE) on the twinning threshold stress for [0 0 1] and [$\bar{1}$ 3 4].

void surface. The critical stress for the dislocation emission is found to decrease with an increasing void size, so that less stress is required to emit dislocations from larger than smaller voids.

Fig. 27 shows SEM images of (a) the initial specimen and (b) the recovered specimen with the bulged top surface. The laser was applied to the lower surface. The reflected tensile pulse at about 100 μm from the real surface can be calculated from the decay of the shock pulse. It is equal in magnitude, but opposite in sign, to the shock pressure. The latter is about 5 GPa in magnitude. Voids were observed in the cross-section. They ranged in size from 25–50 nm to 1 μm. Fig. 28 is a TEM image showing what is believed to be a void near the back surface of the shocked specimen. Its diameter is approximately 0.5 μm. It may be argued that electropolishing produced the void, but a larger number of perforations were found close to the back surface of the specimen, where void formation is expected. There is a light rim around the void, indicating an extremely high dislocation density, beyond the point where individual dislocations can be imaged. This void is similar to the one observed earlier by Christy et al. [43] using high-voltage transmission electron microscopy. In that experiment, the foil was not perforated and the same intense dislocation density was observed. The diameter of this work-hardened layer is approximately twice the void diameter. Thus, a much higher dislocation density characterizes the region surrounding the void compared to regions without observable voids.

3.6. Dislocation emission and void growth

Void growth is indeed a non-homogeneous plastic deformation process. The plastic strains decrease with increasing distance from the void center. The far-field strains are purely elastic, whereas plastic deformation occurs in the regions adjoining the surface of the void. Ashby [44] developed a formalism for the treatment of a non-homogeneous plastic deformation by introducing the concept of the generation of geometrically necessary dislocations. Two different mechanisms were envisaged by Ashby [44], based on prismatic or shear loop arrays. The void growth situation is quite different from the rigid-particle model used by Ashby [44]. Nevertheless,

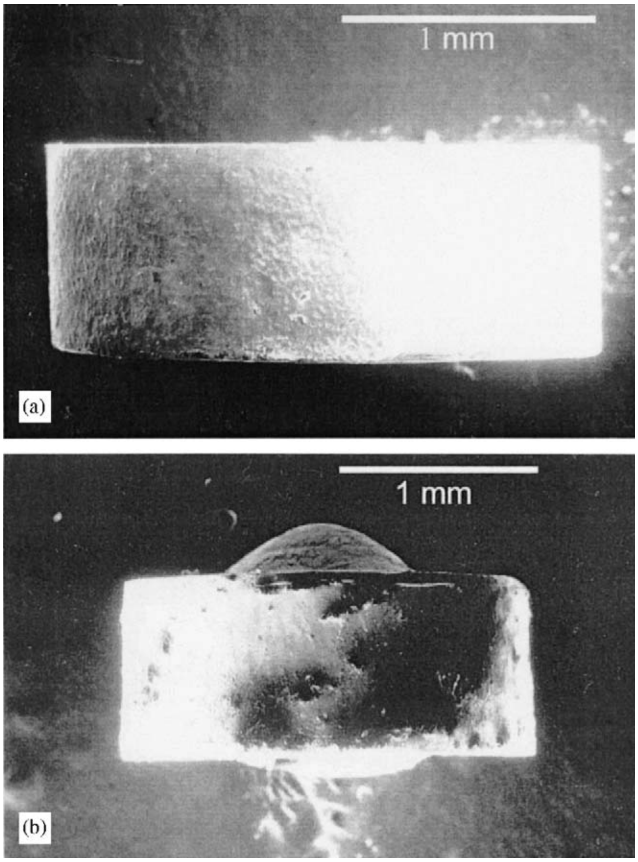

Fig. 27. A side view of the cylindrical specimen subjected to shock compression and subsequent reflected tension pulse from the laser-induced shock wave: (a) undeformed specimen, and (b) deformed specimen upon wave reflection with a created spall surface.

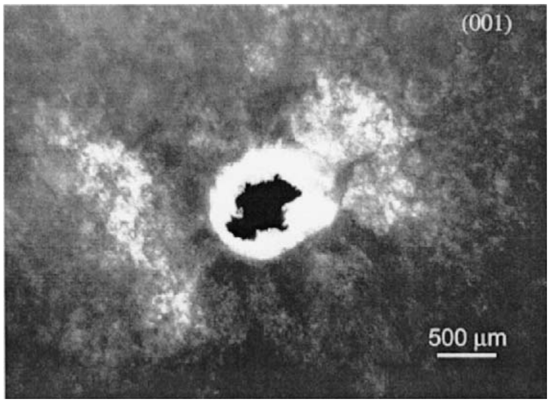

Fig. 28. Dark field image of an isolated void near the rear surface of the specimen and associated work-hardened layer.

it is still possible to postulate arrays of line defects to account for the nonhomogeneous plastic deformation. Of critical importance is the fact that the shear stresses at 45° to the void surface are a maximum, since the normal stresses are zero at the surface of the void. These shear stresses decay to zero at large distances due to the assumption of a far-field hydrostatic stress state. Thus, the shear stresses are highest at the internal surface, obviating dislocation nucleation there. The mechanism of void growth derived by Lubarda et al. [55] for the emission of shear loops will be presented here.

The *shear loop* mechanism involves the emission of dislocations along the slip plane *S*, and is shown in Fig. 29(a). These loops form preferentially at planes intersecting the void along a 45° orientation to the radius. This ensures a 45° angle between the slip plane *S* and the void surface, maximizing the driving force on the dislocation. The difference between this and the Ashby [44] loops is that the two opposite loops have dislocations of the same sign whereas Ashby's [44] opposite loops have opposite signs.

In the two-dimensional case, four pairs of edge dislocations emitted from the surface of a cylindrical void under remote uniform tension give rise to an increase of the average void size by

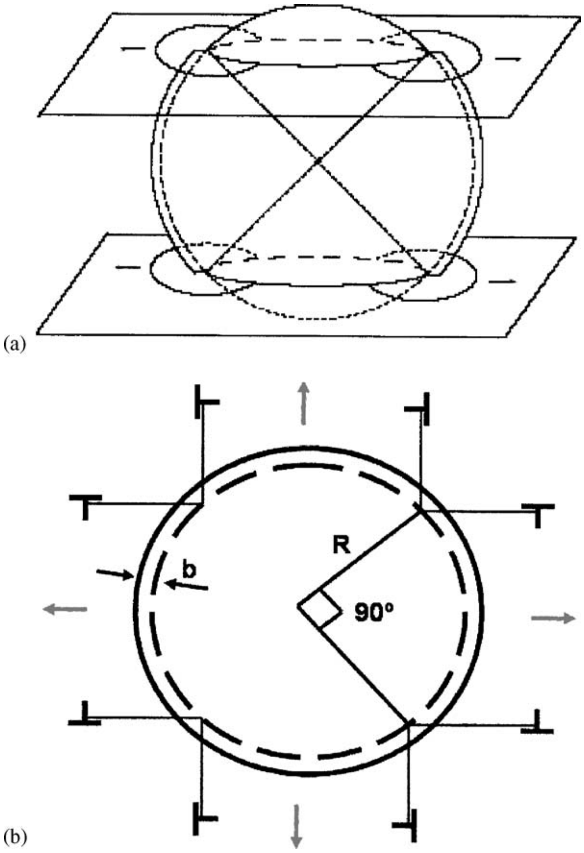

Fig. 29. (a) Emission of two pairs of dislocation shear loops from the void surface along the indicated slip planes, (b) Two-dimensional representation of four pairs of edge dislocations emitted from the surface of a cylindrical void giving rise to an increase of the average void radius by an amount approximately equal to the dislocation Burgers vector.

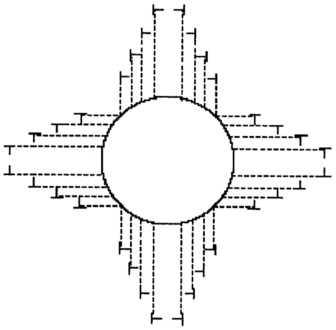

Fig. 30. Network of sequentially emitted dislocations.

an amount approximately equal to the magnitude of the dislocation Burgers vector (Fig. 29(b)). Other arrangements, involving more than four pairs of dislocations, can also be envisioned as giving rise to the expansion of the void [45]. After the void has grown a finite amount, the network of sequentially emitted dislocations may appear as depicted in Fig. 30. In an analytical treatment of the void growth by dislocation emission, we consider the emission of a single dislocation and a single dislocation pair (shear loop) from the surface of a cylindrical void under far-field biaxial tension. The critical stress required for the emission of a shear loop is calculated as a function of the material properties and the initial size of the void. The analysis is based on the criterion adopted from a related study of the crack blunting by dislocation emission (Rice and Thomson [46]). It is shown that the critical stress for the dislocation emission decreases with an increasing void size, so that less stress is required to emit dislocations from larger than smaller voids. At constant remote stresses, this would imply an accelerated void growth by continuing expulsion of shear dislocation loops. However, this is opposed by an increasingly thick work-hardened layer.

3.6.1. Edge dislocation near a cylindrical void

The two-dimensional problem was solved analytically by Lubarda et al. [55] and is presented here in a succinct fashion. Consider an edge dislocation near a cylindrical void of radius R in an infinitely extended isotropic elastic body. The dislocation is at the distance d from the stress-free surface of the void, along the slip plane parallel to the x axis. The stress and deformation fields for this problem have been derived by Dundurs and Mura [47,54]. The interaction energy between the dislocation and the void is:

$$E_{\text{int}} = \frac{Gb^2}{4\pi(1-\nu)}\left[\frac{x^2}{(x^2+y^2)} + \ln\left(\frac{x^2+y^2}{x^2+y^2-R^2}\right)\right], \quad y = \frac{R}{\sqrt{2}}, \tag{16}$$

where b is the magnitude of the Burgers vector of the dislocation, G is the elastic shear modulus, and ν is Poisson's ratio of the material. The shear stress along the considered slip plane acting on a dislocation due to the pressure of the far-field hydrostatic stress σ is equal to [48]:

$$\tau = \sqrt{2}\sigma\frac{\xi}{(\xi+1/2)^2}, \tag{17}$$

where $\xi = x/R$.

The total force on the dislocation due to both the applied stress and the interaction with the void (derivative of Eq. (16)) is

$$\frac{F_x(\xi)}{Gb} = \frac{\xi}{(\xi^2+1/2)^2}\left(\sqrt{2}\frac{\sigma}{G} - \frac{1}{\pi(1-\nu)}\frac{b}{R}\frac{\xi(\xi^4+1/4)}{(\xi^4-1/4)}\right). \tag{18}$$

The normalized force vs. the normalized distance d/b plot, where $d = x - R/(2^{0.5})$, is shown in Fig. 31, in the case when $R = 10b$, $\sigma = 0.1G$ and $\nu = 0.3$. The dislocation position is under unstable equilibrium at $d \approx 2.11b$. For d smaller than $2.11b$, the dislocation is attracted to the void. In the limit $d/b \to \infty$, the dislocation force vanishes since the dislocation is far from the void, which finds itself in the field of uniform biaxial tension σ.

In the equilibrium dislocation position, the attraction from the void is balanced by the applied stress, so that the force $F_x(\xi)$ in Eq. (18) vanishes, i.e.,

$$\sqrt{2}\sigma\frac{\xi}{(\xi^2+1/2)^2} = \frac{G}{\pi(1-\nu)}\frac{b}{R}\frac{\xi(\xi^4+1/4)}{(\xi^2+1/2)^2(\xi^4-1/4)}. \tag{19}$$

This was done using the Rice and Thomson [46] criterion for the spontaneous emission of dislocation from the crack tip. The stress required to emit the dislocation is

$$\frac{\sigma_{\mathrm{cr}}}{G} \geqslant \frac{b/R}{\sqrt{2}\pi(1-\upsilon)}\frac{(1+\sqrt{2}\rho b/R)^4+1}{(1+\sqrt{2}\rho b/R)^4-1}. \tag{20}$$

The plot of σ_{cr}/G vs. R/b is shown in Fig. 32 for a selected value of the material parameter $\rho = 1.5$. The results are meaningful for sufficiently large sizes of voids, typically $R > 3\rho b$ (R greater than $3b$–$6b$). The critical stress required for the dislocation emission decreases with both ρ and R/b. The smaller the dislocation width, the higher the applied stress must be to keep the dislocation in equilibrium near the void. It is noted that the force on the dislocation at a given equilibrium distance from the void due to a remote stress increases more rapidly with the ratio R/b than does the force due to attraction from the void surface. More involved dislocation models

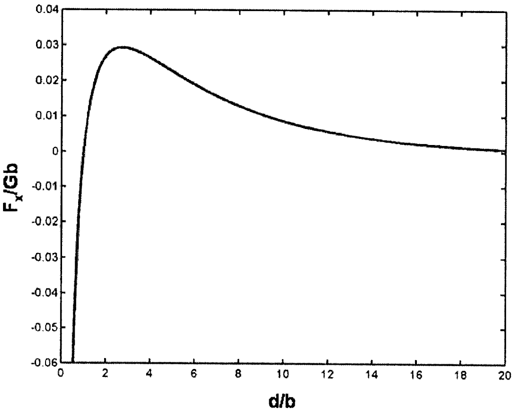

Fig. 31. Normalized dislocation force $F_x = Gb$ vs. normalized distance from the void d/b, according to Eq. (18), for $R = 10b$, $\sigma = 0.1\,G$ and $\nu = 0.3$. The dislocation is in an unstable equilibrium position at $d/b = 2.1$.

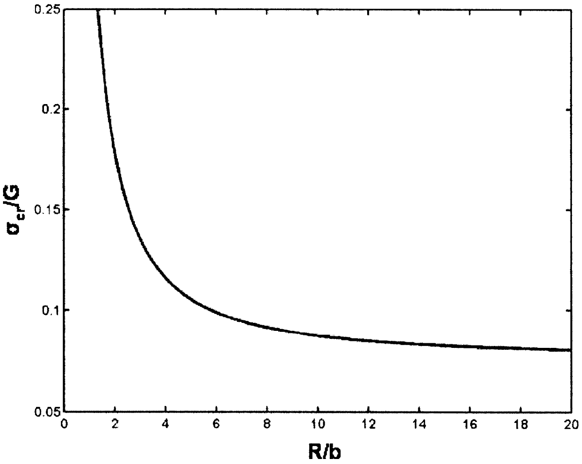

Fig. 32. Normalized critical stress $\sigma_{cr} = G$ required to emit a dislocation from the surface of the void vs. normalized radius of the void $R = b$, according to Eq. (20) ($\nu = 1/3$, $\rho = 1.5$).

based on the Peierls–Nabarro concept, as used by Rice [49] and Rice and Beltz [50] to study the crack blunting by dislocation emission, or by Xu and Argon [56] in their study of the homogeneous nucleation of dislocation loops in perfect crystals, may be needed to further study and improve the analysis of the void growth by dislocation emission. Experimental data in the literature (e.g., Minich et al. [51]) indicates that the spall strength of high purity Cu single crystals is about 5 GPa. The spall strength of a polycrystalline Cu is about half that value, because of grain boundaries and intercrystalline defects which promote void growth. Zurek and Meyers [52] and Meyers [53] discuss the effects of polycrystallinity and grain size on void growth during spall experiments and reconcile the contradictory results. The higher spall strength observed for monocrystalline copper is due to different nucleation sites. In polycrystals, there is segregation of impurities at the grain boundaries, providing favorable initiation sites. In monocrystals, these sites are absent and initiation must occur from vacancy complexes.

3.7. Tri-dimensional modeling of void growth

The tridimensional picture is somewhat more complex than the two-dimensional one. Dislocation loops are emitted circumfrentially around a void, along a plane intersecting it at 45°. Six loops, corresponding to the edge dislocations with directions $[1\,\bar{1}\,0]$, $[1\,0\,\bar{1}]$, $[0\,1\,\bar{1}]$, $[\bar{1}\,1\,0]$, $[\bar{1}\,0\,1]$, and $[0\,\bar{1}\,1]$, are shown in Fig. 33(a). As they expand, their extremities approach each other and eventually react, although this is not energetically favorable under zero-stress conditions:

$$Gb_1^2 + Gb_2^2 < Gb_7^2. \tag{21}$$

The dislocations that form on reaction have a screw character. Successive loops can form on the same $(1\,1\,1)$ plane, as shown in Fig. 33(c), or on adjacent planes, as the void grows. The intersection of a void with eight $\{1\,1\,1\}$ at 45° forming an octahedron, is shown in Fig. 34. The dislocation interactions become rather complex at that level.

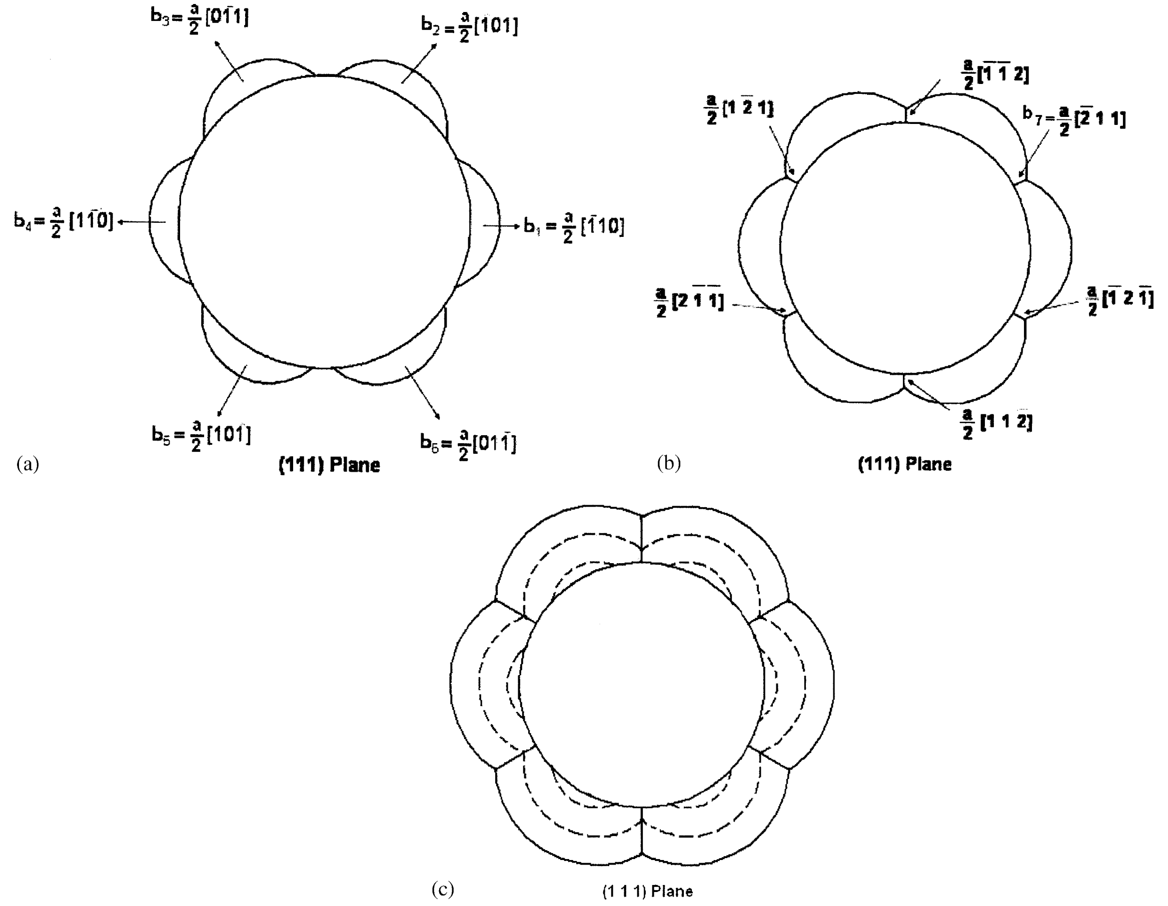

Fig. 33. (a) Three pairs of edge dislocations; (b) reactions between adjacent dislocation loops as they expand; (c) successive emissions of loops.

4. Conclusions

Laser-driven shock compression experiments provide unique information on the process of defect generation at high strain rates. The results obtained in a sustained collaborative program between UCSD and LLNL researchers demonstrate that all critical processes of defect generation operate at the shock front. The pulse duration in the current experiments was on the order of nanoseconds, two orders of magnitude lower than plate impact experiments. Nevertheless, the substructures observed by transmission electron microscopy are very similar.

The threshold pressure for mechanical twinning is calculated and compared with experimentally observed values. The threshold stress was calculated as a function of temperature, for two crystallographic orientations: [1 3 4] and [0 0 1] . This was done as a function of stacking-fault energy, and the threshold stress decreases with stacking-fault energy. Experiments carried out on Cu–2%Al and Cu6%Al confirm the increased predisposition toward stacking-fault and twin

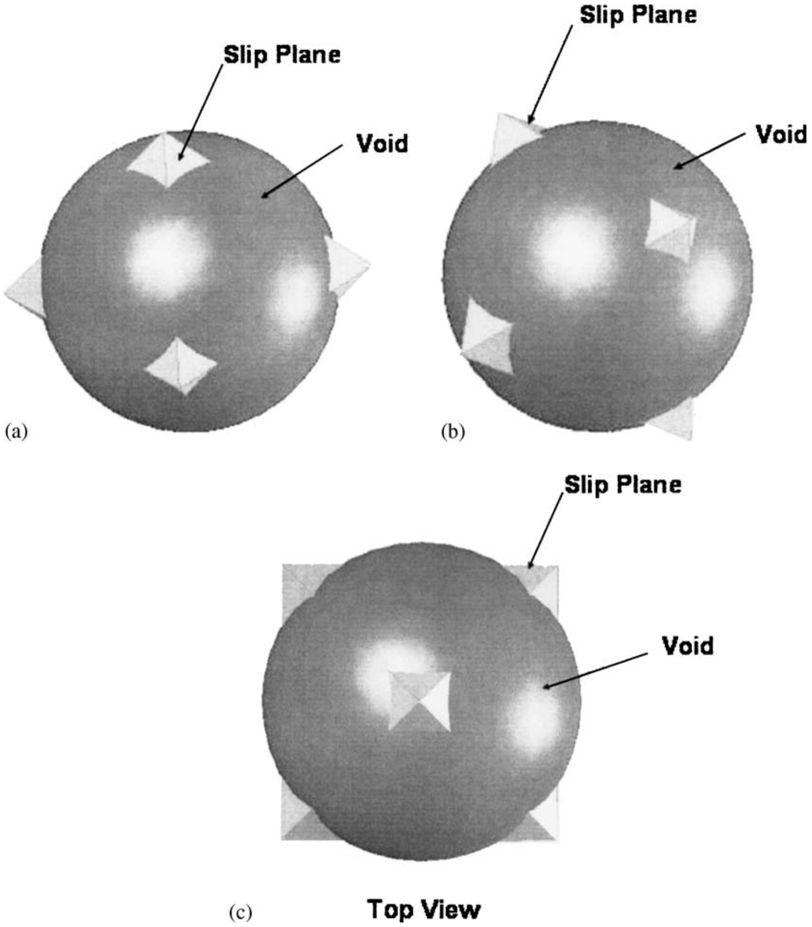

Fig. 34. (a) 3-D model of spherical void intercepting the 8 slip planes that form an octahedron. (b) Another view of the 3-D model of spherical void intercepting the 8 slip planes. (c) Top view of 3-D model.

formation as the stacking-fault energy is decreased. The predicted results compare favorably with experimental observations.

A brief description is presented of a mechanism for void growth under the dynamic conditions propitiated by the reflected shock wave at a free surface. The growth is assumed to occur through the nucleation of shear loops at the void surface and their subsequent expansion.

Acknowledgements

This research was supported by the Department of Energy through Grants DEFG0398DP00212 and DEFG0300SF2202. We thank Prof. V. Lubarda for his contributions to void growth.

References

[1] Smith CS. Trans AIME 1958;212:574.
[2] Askaryon GA, Morez EM. JETP Lett 1963;16:1638.
[3] White RM. J Appl Phys 1963;34:2123.
[4] Bell CE, Landt JA. Appl Phys Lett 1967;10:46.
[5] Panarella E, Savic P. Can J Phys 1968;46:143.
[6] Skeen CH, York CM. J Appl Lett 1968;12:369.
[7] Anderholm NC. Appl Phys Lett 1970;12:113.
[8] Clauer AH, Holbrouk JH, Fairand BP. In: Meyers MA, Murr LE, editors. Shock waves and high-strain-rate phenomena in metals. New York: Plenum Press; 1981. p. 675.
[9] Fairand BP, Clauer AH, Jung RG, Wileot BA. Appl Phys Lett 1974;25:431.
[10] Boustie M, DeResseguier T, Hallouin M, Migault A, Romain JP, Zagouri D. Laser Particle Beams 1996;14:225.
[11] Yabe T, Phipps C, Yamaguchi M, Nakagawa R, Aoki K, Mine H, et al. Appl Phys Lett 2002;80:4318.
[12] Rink K, Delacretaz G, Salathe RP. Appl Phys Lett 1992;61:2644.
[13] Romain JP, Zagouri D. In: Murr LE, Staudhammer KP, Meyers MA, editors. Metallurgical applications of shock-wave and high-strain rate phenomena. New York: Marcel Dekker; 1986. p. 408.
[14] Paisley DL, Warnes RH, Kopp RA. In: Schmidt SC, Dick RD, Forbes JW, Tasker DG, editors. Shock compression of condensed matter 1991. Amsterdam: Elsevier; 1992. p. 825.
[15] Labaste JL, Doucet M, Joubert P. In: Schmidt SC, Shaner JW, Samara GA, Ross M, editors. Shock compression of condensed matter 1995. New York: AIP; 1994. p. 1213.
[16] Johnson Q, Mitchell A, Keeler RN, Evans L. Phys Rev Lett 1970;25:109.
[17] Zaretsky E. J Appl Phys 1995;78:1.
[18] Wark JS. Phys Rev B 1989;40:5705.
[19] Kalantar DH, Chandler EA, Colvin JD, Lee R, Remington BA, Weber SV, et al. Rev Sci Instrum 1999; 170:629.
[20] Kalantar DH, Belak J, Bringa E, Budil K, Caturla M, Colvin J, et al. Phys Plas 2003;10:1569.
[21] Kalantar DH, Bringa E, Caturla M, Colvin J, Lorenz KT, Kumar M, et al. Rev Sci Instrum 2003;74:1929.
[22] Meyers MA, Gregori F, Kad BK, Schneider MS, Kalantar DH, Remington BA, et al. Acta Mat 2003;51:1211.
[23] Meyers MA, Murr LE. Shock waves and high-strain-rate phenomena in metals. New York: Plenum Press; 1981 (Appendices).
[24] Tong W, Clifton RJ, Huang S. J Mech Phys Sol 1992;40:1251.
[25] Zerilli FJ, Armstrong RW. J Appl Phys 1987;61:1816.
[26] Follansbee PS, Gray III GT. Mat Sci Eng 1991;138:23.
[27] Murr LE. In: Meyers MA, Murr LE, editors. Shock waves and high-strain-rate phenomena in metals. New York: Plenum Press; 1981. p. 607.
[28] Murr LE. Scripta Metall 1978;12:201.
[29] Johari O, Thomas G. Acta Metall 1964;12:1153.
[30] Murr LE. Interfacial phenomena in metals and alloys. Reading, MA: Addison-Wesley; 1975. p. 142.
[31] Gallagher PCJ. Met Trans 1970;l:2429.
[32] Thomas G. Acta Metall 1965;13:1211.
[33] Murr LE, Meyers MA, Niou CS, Chen YJ, Pappu S, Kennedy C. Acta Mater 1997;45:157.
[34] Meyers MA, Voehringer O, Lubarda VA. Acta Mater 2001;49:4025.
[35] Swegle JW, Grady DE. J Appl Phys 1983;58:941.
[36] Follansbee PS. In: Murr LE, Staudhammer KP, Meyers MA, editors. Metallurgical applications of shock-wave and high-strain rate phenomena. New York: Marcel Dekker; 1986. p. 451.
[37] Meyers MA, Benson MA, Voehringer O, Kad BK, Xue Q, Fu HH. Mat Sci Eng 2002;A322:194.
[38] Vöhringer O. Z Metallk 1976;67:51.
[39] Kan T, Haasen P. Mat Sci Eng 1969–1970;5:237.
[40] Labusch R. Phys Status Solidi 1970;41:659.
[41] Jax P, Kratochvil P, Haasen P. Acta Metall 1970;18:237.

[42] Rohatgi A. A microstructural investigation of shock loading effects in FCC materials. PhD thesis, University of San Diego, California, 1999.

[43] Christy S, Pak HR, Meyers MA. In: Meyers MA, Murr LE, Staudhammer KP, editors. Shock-wave and high-strain-rate phenomena in materials. New York: Marcel Dekker, Inc.; 1986. p. 835.

[44] Ashby MF. Philos Mag 1970;21:399.

[45] Hahn GT, Flanagan WF. In: Ashby MF, Bullough R, Hartley CS, Hirth JP, editors. Dislocation modeling of physical systems. Oxford: Pergamon Press; 1980. p. 1.

[46] Rice JR, Thomson R. Philos Mag A 1974;29:73.

[47] Dundurs J, Mura TJ. Mech Phys Solids 1964;12:177.

[48] Timoshenko S, Goodier JN. Theory of elasticity. New York: McGraw-Hill; 1951.

[49] Rice JR. J Mech Phys Solids 1992;40:239.

[50] Rice JR, Beltz GE. J Mech Phys Solids 1994;42:333.

[51] Minich RW, Kumar M, Cazamia J, Schwartz AJ. Dynamic deformation: constitutive modeling, grain size, and other effects. San Diego: 2003 TMS Annual Meeting; 2003.

[52] Meyers MA, Zurek AK. In: Davison L, Grady DE, Shahinpoor M, editors. High pressure shock compression of solids II. New York: Springer; 1995. p. 25.

[53] Meyers MA. In: Meyers MA, Armstrong RW, Kirchner HOK, editors. Mechanics and materials: fundamentals and linkages. Amsterdam: Elsevier; 1999. p. 489.

[54] Dundurs J. In: Mura T, editor. Mathematical theory of dislocations. New York: ASME; 1969. p. 70.

[55] Lubarda VA, Schneider MS, Kalantar DH, Remington BA, Meyers MA. Acta Mat 2004;52:1397.

[56] Xu G, Argon AS. Philos Mag Lett 2000;80:605.

[57] Diehl J. Z Metallk 1956;47:331.

[58] De Angelis RJ, Cohen JB. J Met 1963;15:681.

[59] Gray III, GT. In: Meyers MA, Murr LE, Staudhammer KP, Dekker M, editors. Shock-Wave and High-Strain-Rate Phenomena in Materials. New York; 1992. P. 899–902.